

1 **Variations in Boundary Layer Stability Across Antarctica: A Comparison**  
2 **Between Coastal and Interior Sites**

3 Mckenzie J. Dice <sup>1,2,3</sup>

4 John J. Cassano <sup>1,2,3</sup>

5 Gina C. Jozef <sup>1,2,3</sup>

6 Mark Seefeldt <sup>2,3</sup>

7 <sup>1</sup> Department of Atmospheric and Oceanic Sciences, University of Colorado Boulder

8 <sup>2</sup> Cooperative Institute for Research in Environmental Sciences, University of Colorado Boulder

9 <sup>3</sup> National Snow and Ice Data Center, University of Colorado Boulder

10 **Key points**

- 11
- 12
- 13
- 14
- 15
- 16
- 17
- 18
- 19
- 20
- Self-organizing maps are used to examine the range of boundary layer stability profiles at two continental and three coastal Antarctic sites.
  - Near neutral to weak near surface stability usually occurs half or more than half of the time in all seasons at the coastal sites but is infrequent at continental interior sites, except in the summer.
  - When considering maximum stability near the surface or just above the boundary layer moderate or stronger stability occurs almost always at the interior sites and often more than half of the time at the coastal sites.
  - At two of the three coastal sites analyzed here, moderate and strong stability occur more often with clear than cloudy sky conditions at one of the coastal sites near neutral and weak stability regimes occur more often with cloudy conditions.

*Correspondence to:* Mckenzie Dice, [mckenzie.dice@colorado.edu](mailto:mckenzie.dice@colorado.edu)

21 **Abstract.** The range of boundary layer stability profiles, from the surface to 500 m above ground level,  
22 present in radiosonde observations from two continental interior (South Pole and Dome Concordia) and  
23 three coastal (McMurdo, Georg von Neumayer III, and Syowa) Antarctic sites, is examined using the self-  
24 organizing maps (SOMs) neural network algorithm. A wide range of potential temperature profiles is  
25 revealed, from shallow boundary layers with strong near-surface stability to deeper boundary layers with  
26 weaker or near neutral stability, as well as profiles with weaker near-surface stability and enhanced  
27 stability aloft, above the boundary layer. Boundary layer regimes were defined based on the range of  
28 profiles revealed by the SOM analysis. Twenty boundary layer regimes were identified to account for  
29 differences in stability near the surface as well as above the boundary layer. Strong, very strong, or  
30 extremely strong stability, with vertical potential temperature gradients of 5 to in excess of 30 K (100 m)  
31 <sup>-1</sup>, occurred more than 80% of the time at South Pole and Dome Concordia in the winter. Weaker stability  
32 was found in the winter at the coastal sites, with moderate and strong stability (vertical potential  
33 temperature gradients of 1.75 to 15 K (100 m)<sup>-1</sup>) occurring 70% to 85% of the time. Even in the summer,  
34 moderate and strong stability is found across all five sites, either immediately near the surface or aloft,  
35 just above the boundary layer. While the mean boundary layer height at the continental interior sites was  
36 found to be approximately 50 m, the mean boundary layer height at the coastal sites was deeper, around  
37 110 m. Further, a commonly described two stability regime system in the Arctic associated with clear or  
38 cloudy conditions was applied to the 20 boundary layer regimes identified in this study to understand if  
39 the two-regime behavior is also observed in the Antarctic. It was found that moderate and strong stability  
40 occur more often with clear than cloudy sky conditions, but weaker stability regimes occur almost equally  
41 for clear and cloudy conditions.

## 42 **1 Introduction**

43 Strong temperature inversions in Antarctica are the result of predominantly high albedo ice-  
44 covered surfaces and low sun angle in the summer and polar night in winter. All these factors contribute  
45 to prolonged surface radiative cooling which often results in statically stable boundary layers (King and  
46 Turner, 1997; Andreas et al., 2000) with temperature inversions sometimes exceeding 20 K (Lettau and  
47 Schwerdtfeger, 1967; Phillpot and Zillman, 1970; Connolley, 1996). Increased solar radiation and warmer  
48 surface temperatures can result in near neutral or weakly stable conditions during the summer. Similar  
49 stability conditions can also occur at other times of year as a result of increased wind speeds or increased  
50 downwelling longwave radiation due to cloud cover (Hudson and Brandt, 2005; Stone and Kahl, 1991).  
51 This study aims to investigate the range of boundary layer stability that exists throughout the year at two  
52 continental interior sites and three coastal sites in Antarctica (Figure 1).

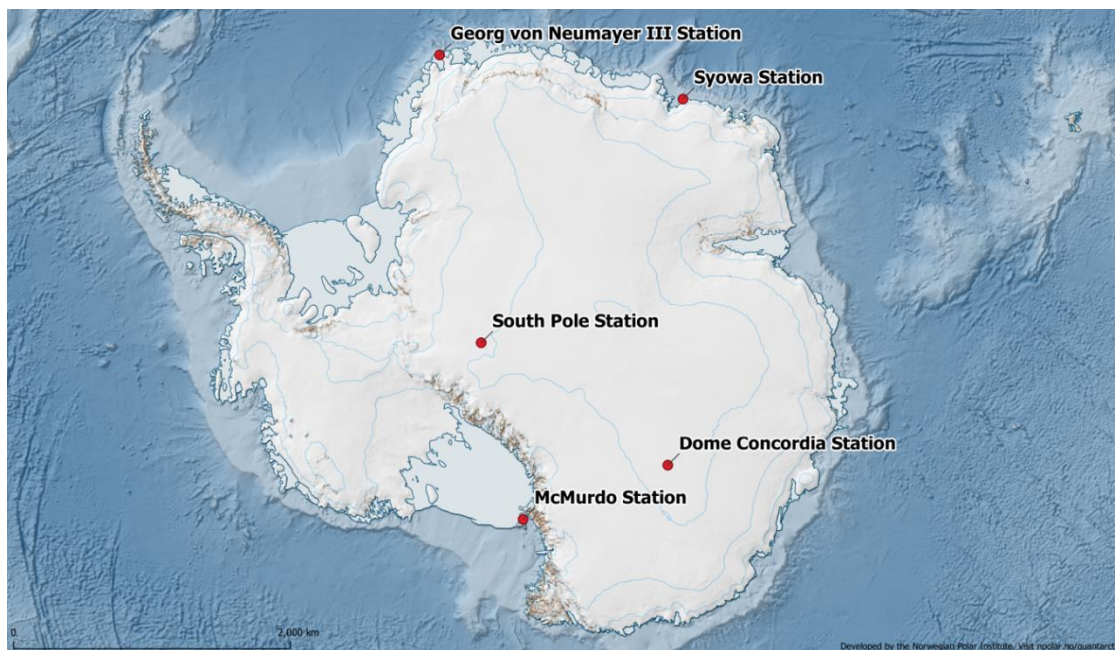
53 A previous study for McMurdo Station analyzed the range of boundary layer stability regimes  
54 present during the year-long Department of Energy (DOE) Atmospheric Radiation Measurement (ARM)  
55 West Antarctic Radiation Experiment (AWARE) campaign (Dice and Cassano, 2022). A strong  
56 seasonality of varying boundary layer stability was found, with the winter conditions dominated by  
57 strongly stable boundary layers (61% of the time), and summer conditions dominated by weak stability  
58 (83% of the time). Increased wind speeds in the winter were found to be responsible for reducing strong  
59 near-surface stability. This reduction of stability occurred near the surface while enhanced stability  
60 remained aloft in some cases. The results presented below aim to expand the analysis of boundary layer  
61 stability in Dice and Cassano (2022) to both continental and coastal locations across Antarctica.

62 Data from two additional coastal stations, Georg von Neumayer Station III (Neumayer Station)  
63 and Syowa Station (Figure 1) will also be analyzed, in addition to revisiting the data at McMurdo Station  
64 described above. Previously published results found surface-based temperature inversions occurred year-  
65 round at Neumayer Station, with a maximum frequency in the winter and a minimum in the summer, with  
66 75% of the inversions having a strength of more than 1 K, and some up to 25 K, especially in the winter  
67 (König-Langlo and Loose, 2007; Silva et al., 2022). Some of the temperature profile structures observed  
68 by Silva et al. (2022) revealed multiple inversions within the same profile. This is similar to McMurdo  
69 Station where enhanced stability was often found to exist above a layer of weaker stability (Dice and  
70 Cassano, 2022). Cassano et al. (2016) found that stable boundary layer conditions occur 83% of the year  
71 over the northwestern Ross Ice Shelf (approximately 100 km from McMurdo Station), while neutral  
72 conditions occur 17% of the time. Further, 50% of the summer season was characterized by weakly  
73 unstable conditions, while stable stratification is dominant in the other three seasons (84% to 94%).

74 The continental interior of Antarctica is characterized by a short summer and a long, coreless  
75 winter (Hudson and Brandt, 2005). Stronger inversions and colder temperatures are often characteristic of  
76 higher elevation, continental interior sites (Phillpot and Zillman, 1970; Comiso, 1994; Zhang, et al.,  
77 2011), compared to coastal locations with weaker inversions and warmer temperatures (Phillpot and  
78 Zillman, 1970; Cassano et al., 2016). Continental interior sites also have greater inversion frequency than  
79 coastal sites, with inversion frequency in the fall and winter close to 100% (Zhang et al., 2011). At South  
80 Pole Station, inversions were found to be more common and stronger in the winter than in the summer.  
81 Hudson and Brandt (2005) also found inversions in the summer at Dome C to be stronger than those at  
82 South Pole. Inversions near the surface at Dome C can reach to  $1 \text{ K m}^{-1}$  during polar night, and even  
83 stronger inversions, at 10 to 15 m above the surface, of up to  $2.5 \text{ K m}^{-1}$  have been observed (Genthon et  
84 al., 2013).

85 Boundary layer stability in the polar regions in the winter has often been described as existing in  
86 two distinct states (weak or strongly stable) driven by changes in cloud cover. The weakly stable regimes  
87 occur under cloudy conditions, with increased downwelling longwave radiation warming the surface and  
88 reducing stability. Cloudy conditions can also result cloud-top radiative cooling and initiate convective  
89 mixing when the atmosphere is cooled aloft by the cloud (Chechin et al., 2023). In contrast, clear sky  
90 conditions allow for strong radiative cooling and strong stability (Stone and Kahl, 1991; Mahrt et al.,  
91 1998; Mahrt, 2014; Solomon et al., 2023). Stone and Kahl (1991) described boundary layer stability at the  
92 South Pole as being in either a weakly stable or strongly stable regime, associated with cloudy or clear  
93 conditions, respectively throughout the summer of 1986. Solomon et al. (2023) distinguished between  
94 wintertime clear and cloudy regimes in the Arctic, during the Multidisciplinary drifting Observatory for  
95 the Study of Arctic Climate (MOSAIC) campaign, to evaluate model predictions of near-surface  
96 meteorological conditions including boundary layer stability. They separated clear and cloudy regimes  
97 using the minima between the two peaks in the observed bimodal probability distribution function (PDF)  
98 of net longwave radiation. Following Solomon et al. (2023) we will identify clear and cloudy regimes  
99 based on the PDFs of net longwave radiation to determine if this bimodal view of clouds, and associated  
100 boundary layer stability, found in the Arctic is also applicable to coastal and interior sites across the  
101 Antarctic continent. We will also study how the clear-cloudy regimes relate to the continuous range of  
102 stability regimes identified in this study.

103 This paper begins with a description of the observations from five Antarctic sites and details of  
104 the methods used to analyze the data at these sites (Section 2). The results of this analysis will describe  
105 the range and frequency of boundary layer stability profiles (up to 500 m AGL) at the sites (Section 3).  
106 Additionally, differences in boundary layer stability associated with clear and cloudy conditions will be  
107 presented. The results section will be followed by a discussion and comparison across coastal versus  
108 continental interior locations (Section 4). A summary of these findings will follow, and the next steps in  
109 this research will be identified (Section 5).



110 *Figure 1: Location of study sites (red dots with station names) across the Antarctic continent. Map*  
111 *courtesy of Quantarctica (Matsuoka et al., 2018).*

## 112 **2 Data and Methods**

### 113 **2.1 Data**

114 The analysis presented in this paper is based on radiosonde and surface longwave radiation  
115 observations from three coastal (McMurdo Station, Neumayer Station, and Syowa Station) and two  
116 continental interior sites (South Pole Station, Dome Concordia Station) (Figure 1, Table 1, hereafter these  
117 five stations are referred to as McMurdo, Neumayer, Syowa, South Pole, and Dome C). The period of  
118 data used in the analysis at these five sites range from 13 months (McMurdo) to 19 years (Syowa). The  
119 differing time period evaluated at each site is due to varying amounts of time when radiosonde and  
120 radiation data are both continuously available, as well as periods of time when data was readily  
121 accessible. At McMurdo, this time period was chosen to coincide with availability of both radiosonde and  
122 radiation data from the AWARE campaign, which was previously analyzed by Dice and Cassano (2022).  
123 The Neumayer dataset is shorter than those at Syowa, Dome C, and South Pole, as Neumayer was not  
124 fully operational until 2009, and from 2009 to 2018, only 5 s temporal resolution radiosonde data was  
125 available. This data did not have sufficient vertical resolution for this study, thus only data after 2018 with  
126 1 s temporal resolution was used. Syowa, Dome C, and South Pole all have longer continuous radiosonde  
127 and radiation datasets, that are easily accessible, lasting more than approximately 15 years.

128 South Pole is a high-elevation (2,835 m) continental interior site where strong surface inversions  
129 and extremely cold temperatures dominate (Zhang et al., 2011), and strong stability is almost constantly  
130 observed, especially in the winter (Phillpot and Zillman, 1970). The radiosonde data from the South Pole  
131 were retrieved from the Antarctic Meteorological Research and Data Center from 1 January 2005 to 29  
132 September 2021. Radiosonde launches occur once daily at 2100 UTC for most of the year, with twice  
133 daily launches at approximately 0900 UTC and 2100 UTC during the short austral summer. These  
134 launches occur at 2200 and 1000 local time, respectively.

135 Dome C is another high-elevation (3,233 m) continental interior site characterized by cold  
136 temperatures and strong surface inversions, which occur throughout most of the year, and in the winter on  
137 a nearly permanent basis (Genthon et al., 2013; Pietroni et al., 2014, Vignon et al., 2017). The radiosonde  
138 data from Dome C are provided by the Antarctic Meteo-Climatological Observatory from 21 January  
139 2006 to 14 October 2021. The radiosonde launches at Dome C are performed once daily at 1200 UTC  
140 year-round. It is important to note here that the 1200 UTC soundings are 0400 local time, which is early  
141 morning at Dome C. Thus, at this time, the profiles from the radiosondes are likely to be reflective of  
142 shallower, more stable boundary layer conditions, rather than convective which is sometimes observed in  
143 near surface observations during mid-day or in the summer at Dome C (Mastrantonio, et al., 1999;  
144 Pietroni et al., 2013).

145 McMurdo is a coastal site located at the edge of the Ross Ice Shelf on the southwestern tip of  
146 Ross Island. The proximity of the Ross Ice Shelf, sea ice, open water, and the complex local topography  
147 near McMurdo results in a wide range of boundary layer stability types compared to the continental  
148 interior sites (Dice and Cassano, 2022). The McMurdo radiosonde data are from the DOE AWARE  
149 campaign (Lubin et al., 2017, 2020; Silber et al., 2018), which occurred at McMurdo from 20 November  
150 2015 to 3 January 2017. The radiosonde launches during AWARE occurred twice per day at 1000 UTC  
151 and 2200 UTC (2300 and 1100 local time, respectively).

152 Neumayer is near sea-level and located on the Ekström Ice Shelf, a relatively flat and  
153 homogeneous site. The meteorology and near-surface conditions are frequently influenced by large-scale

154 cyclonic activity and sea ice fluctuations (Silva et al., 2022) resulting in changing boundary layer  
155 conditions. The radiosonde data from Neumayer are from the Baseline Surface Radiation Network  
156 (BSRN) from 1 June 2018 to 31 January 2021. Radiosonde launches occur once daily at approximately  
157 1200 UTC, and twice daily during the summer months when conditions allow, at 0500 UTC and 1200  
158 UTC (where UTC is local time).

159 Syowa is located on East Ongul Island in Lutzow-Holm Bay near sea level, with some low-  
160 elevation slopes around it, and like the other coastal sites, it experiences warmer surface temperatures  
161 compared to the continental interior. Syowa also experiences occasional strong wind due to katabatic flow  
162 from the continental interior (Murakoshi, 1958). The radiosonde data from Syowa are from the Office of  
163 Antarctic Observation Japan Meteorological Agency (pers. comm. Yutaka Ogawa) from 1 February 2001  
164 to 23 January 2020. Radiosonde launches occur twice daily at 1130 and 2330 UTC (1430 and 0230 local  
165 time respectively).

166 Longwave radiation data were also obtained for all five sites to identify the clear and cloudy sky  
167 conditions following the methods from Solomon et al. (2023). The radiation data are from the BSRN,  
168 except at McMurdo where the data is from the AWARE campaign.

169 *Table 1: Information for each of the five study sites: South Pole, Dome C, McMurdo, Neumayer, and*  
 170 *Syowa. From left to right, the columns indicate: study site, coordinates and elevation above sea level*  
 171 *(ASL) of each site, site location type, the type of radiosonde and accuracy of the temperature and wind*  
 172 *measurements, respectively, the time period of the radiosonde launches, and the number of radiosonde*  
 173 *launches in the dataset.*

Station	Coordinates, Elevation	Site Type	Instrument Type and Accuracy	Time Period of Radiosonde Launches	Number of Radiosonde Launch Profiles
South Pole	-89.98°S, 24.80°W; 2,836 m ASL	Interior plateau	Vaisala RS41-SGP radiosondes; 0.2 K, 0.5 m s <sup>-1</sup>	01 Jan 2005-29 Sep 2021	8,587
Dome C	-75.10°S, 123.33°E; 3,251 m ASL	Interior plateau	RS-92 radiosondes; 0.2 K, 0.2 m s <sup>-1</sup>	21 Jan 2006- 14 Oct 2021	5,147
McMurdo	-77.85°S, 166.66° E; 10.1 m ASL	Coastal; Ross Island	RS-92 radiosondes; 0.2 K, 0.2 m s <sup>-1</sup>	30 Nov 2015- 03 Jan 2017	786
Neumayer	-70.65°S, - 8.17°W; 38 m ASL	Coastal; Ekström Ice Shelf	Vaisala, RS41-SGP radiosondes; 0.2 K, 0.5 m s <sup>-1</sup>	01 Jun 2018- 31 Jan 2021	1,220
Syowa	-69.00°S, 39.58°W; 18.4 m ASL	Coastal; East Ongul Island	Meisei RS-11G radiosondes; 0.5 K, 2 m s <sup>-1</sup>	01 Feb 2007- 23 Jan 2020	6,390

## 174 2.2 Methods

### 175 2.2.1 Self-Organizing Map

176 The goal of this paper is to analyze and compare the variability in boundary layer stability,  
 177 defined by potential temperature profiles, at five Antarctic research stations (Figure 1). Hundreds to  
 178 thousands of radiosonde profiles (Table 1), for each of the five sites, will be analyzed. The self-organizing  
 179 map, or SOM, algorithm is used to objectively identify patterns in the potential temperature profiles that  
 180 represent the range of conditions in the radiosonde observations.

181 The SOM algorithm is an unsupervised artificial neural network that groups similar patterns in  
 182 the training data into a user-specified number of patterns, which span the range of conditions in the  
 183 training data. The iterative training proceeds until the squared difference between the training data and the  
 184 SOM patterns is minimized (Kohonen et al., 1996; Hewitson and Crane, 2002; Cassano et al., 2015). The  
 185 resulting two-dimensional array of patterns is the master SOM, or simply the SOM. The SOM is  
 186 organized such that similar patterns are located adjacent to each other, while the most distinct patterns are

187 on opposite sides (Cassano et al., 2016). The SOMs presented here are trained using potential temperature  
188 gradient profiles from the radiosonde observations. The potential temperature gradient profiles ( $d\theta/dz$ )  
189 were used to train the SOM because this gradient defines the local static stability in the profile and allows  
190 for classification of boundary layer stability regimes across seasons and sites. The SOMs in this study  
191 were trained using the SOM-PAK software (<http://www.cis.hut.fi/research/som-research>), the details of  
192 which are described by Kohonen et al. (1996).

193 The radiosonde data is interpolated onto a regular vertical grid before applying the SOM  
194 algorithm, as described in Dice and Cassano (2022). Radiosonde profiles from all sites were interpolated  
195 to a 5 m grid from 20 to 500 m above ground level. The lowest height of 20 m was selected since near-  
196 surface warm biased temperatures are often present in radiosonde data observed below this height in  
197 many profiles at the five study sites (Schwartz and Doswell, 1991; Mahesh et al., 1997). The top height of  
198 500 m was chosen since this height encompasses the boundary layer features of interest. It is also  
199 important to note here that the boundary layer in Antarctica has been observed to be shallower, and stable  
200 conditions extend further to the surface, than the 20 m bottom height in the profiles used in this analysis  
201 (e.g., Handorf et al., 1999). However, below this height in the radiosonde profiles, anomalously warm  
202 biased temperatures are important to exclude, since this will indicate weaker stability than are actually  
203 present during the radiosonde launches.

204 To decide on the number of patterns to be identified by the SOM algorithm, several tests were  
205 performed to find the appropriate SOM size to adequately represent the range of boundary layer profiles  
206 present at each of the five sites. Unlike other iterative, unsupervised training algorithms, the SOM does  
207 not identify distinct patterns, but a range of patterns which vary smoothly across the boundary layer states  
208 observed in the radiosonde data. Identifying the proper SOM size is important for visualizing the full  
209 range of boundary layer stability profiles present in the training data (Reusch et al., 2005; Cassano et al.,  
210 2015). Too small of a SOM will result in important differences in the training data being lost in the few  
211 generalized patterns, and too large of a SOM will be difficult to visualize, and only a few samples from  
212 the training data may correspond, or “map” to each SOM pattern. Several SOM sizes were tested for this  
213 analysis: 3 x 2 (6 patterns), 4 x 3 (12 patterns), 5 x 4 (20 patterns), 6 x 5 (30 patterns), and 7 x 6 (42  
214 patterns). This initial evaluation of different SOM sizes found that a 6x5 SOM (Figures 2, 4, 6, 8, and 10)  
215 best represented the boundary layer states present across the training data at all five sites. The 30 patterns  
216 in the 6x5 SOM span the range of potential temperature profile types present in the training data, which  
217 represents the hundreds to thousands of profiles (Table 1) from each of the five sites.

218 Once the SOM is trained, each individual radiosonde profile from the training data is “mapped”  
219 to a single pattern in the SOM that it is most similar to by finding the pattern that has the smallest squared  
220 difference between the radiosonde profile and the SOM-identified pattern. This mapping procedure  
221 produces a list of best matching units, or BMUs, which identify the potential temperature gradient profiles  
222 in the training data that correspond to each pattern in the SOM. Using this list, mean potential temperature  
223 gradient and mean potential temperature anomaly (defined relative to the potential temperature at 500 m)  
224 profiles are calculated and used to visualize the range of stability profiles present at each site (Figures 2,  
225 4, 6, 8 and 10). The list of BMUs is also used to calculate the frequency of occurrence of each SOM  
226 pattern and can be used to identify how boundary layer stability varies annually and seasonally. The  
227 seasons are defined in this study as follows: summer (DJ), fall (FMA), winter (MJJA), and spring (SON).  
228 These seasons are identified as such following previous definitions of Antarctic seasons (Cassano et al.,  
229 2016, Nigro et al., 2017).

230



## 231 2.2.2 Boundary Layer Regime Definitions

232 The SOM analysis described above provides a relatively compact way to visualize the range of  
233 boundary layer conditions present in the radiosonde observations, as well as their seasonality at the  
234 various sites. However, this analysis does not allow for direct, quantitative comparison across the five  
235 sites since unique SOMs are defined for each location, and the results below will show that the range of  
236 stability at each of the five sites is very different. Thus, to compare the range of boundary layer stability  
237 present at each of the five sites (Figure 1) the potential temperature gradient profiles, as shown by the  
238 SOMs at each of the study sites, are used to define boundary layer stability regimes that can be applied  
239 across all of the sites. The stability regime definitions are based on both the near-surface stability (20 m to  
240 50 m) and stability above the height of the boundary layer (up to 500 m) and boundary layer depth.

241 Six near-surface stability regimes were defined (Table 2, left column) based on the potential  
242 temperature gradient between 20 m and 50 m above ground, as this depth captures the near-surface  
243 conditions while avoiding measurement errors below 20 m. The near-surface stability regimes range from  
244 near neutral (NN;  $d\theta/dz < 0.5 \text{ K (100 m)}^{-1}$ ) to extremely strongly stable (ESS;  $d\theta/dz > 30 \text{ K (100 m)}^{-1}$ ).  
245 Various thresholds to distinguish near neutral (NN), weak (WS), moderate (MS), strong (SS), very strong  
246 (VSS), and extremely strong (ESS) stability were evaluated, and the thresholds listed in Table 2 were  
247 found to best separate meaningful differences in near-surface stability across all five sites. These  
248 thresholds were also evaluated, and found to be appropriate, in a separate study based on profiles  
249 observed over Arctic sea ice as part of the MOSAiC expedition (Jozef et al. 2023). It is also important to  
250 note that the NN regime with potential temperature gradients less than  $0.5 \text{ K (100 m)}^{-1}$  may include some  
251 negative potential temperature gradients, thus convective conditions, which, while rare in the Antarctic,  
252 can occur with strong radiative heating during the austral summer, or advection of cold air over a  
253 relatively warmer surface.

254 It was also noted that many of the SOM patterns were characterized by a layer of stronger  
255 stability above weaker stability near the surface, which was also noted by Dice and Cassano (2022) at  
256 McMurdo. Therefore, the stability above the boundary layer is also used to define the overall stability  
257 regime (Table 2). This requires identifying the top of the boundary layer, which is done following Jozef et  
258 al. (2022) by using profiles of the bulk Richardson number. The bulk Richardson number is defined as the  
259 approximation of the ratio of buoyant turbulence production, or suppression, to mechanical generation of  
260 turbulence by wind shear. A critical bulk Richardson number indicates the point at which turbulence  
261 cannot be sustained (Stull, 1988). The boundary layer height is defined as the point in the profile where  
262 the bulk Richardson number exceeds a critical value of 0.5 and remains above that critical value for at  
263 least 20 meters consecutively.

$$R_B = \frac{g\Delta\theta\Delta z}{\bar{\theta}[(\Delta U)^2 + (\Delta V)^2]} \quad \text{Equation 1}$$

264 Where, in Equation 1,  $g$  is the acceleration due to gravity,  $\theta$  is potential temperature,  $U$  is the  
265 zonal wind and  $V$  is the meridional wind,  $\Delta$  indicates the change in variables over the change in altitude  
266 ( $\Delta z$ , 5 m) and the overbar indicates the mean potential temperature over the change in altitude ( $\Delta z$ ).

267 Aloft stability regimes were determined with the same potential temperature gradient thresholds  
268 as were used for the near surface stability regimes (Table 2). The maximum potential temperature  
269 gradient above the boundary layer height and below 500 m was used to identify the aloft stability regimes.  
270 Aloft-stability regimes were applied to any potential temperature gradient profile with a greater stability

aloft compared to the near-surface stability of that profile. No aloft stability regime is applied for cases with the strongest stability near the surface.

Boundary layer stability regimes were also defined based on the depth of the boundary layer. In analyzing all the boundary layer profiles it was found that there was a clear distinction between a group of NN and WS regimes with boundary layer heights less than 125 m, and NN and WS regimes with boundary layer heights much greater than 125 m. Thus, a very shallow mixed (VSM) stability regime was defined to distinguish these cases, specifically for the NN and WS regimes with boundary layer depths less than 125 m.

The near-surface and aloft stability regimes, along with the VSM regimes, were combined into an overall stability regime, as listed in Table 3. For example, a profile identified as having near neutral stability near the surface with strong stability above the boundary layer, would be identified as near neutral, strong stability aloft, or NN-SSA. Thus, we end up with “stability groupings” with the same near surface stability for multiple regimes, but with varying stability aloft. One example of these groupings is the following: NN (near neutral), NN-WSA (near neutral, weak stability aloft), NN-MSA (near neutral, moderate stability aloft), and NN-SSA (near neutral, strong stability aloft; Table 3). The boundary layer stability regimes defined here are then applied to the patterns in the SOMs to show how this definition scheme applies to the range of potential temperature gradient profiles originally identified in the SOM, which was used to inform the development of the boundary layer stability regime definitions.

Table 2: Boundary Layer Regime definition scheme. The left column of the table shows the potential temperature gradient ( $d\theta/dz$  in  $K (100 m)^{-1}$ ) thresholds used to define each of the six basic near-surface stability regimes from 20 m to 50 m. The middle column shows how the very shallow mixed layer definition was applied to NN and WS cases. The third column shows the maximum potential temperature gradient thresholds ( $d\theta/dz$  in  $K (100 m)^{-1}$ ) for the aloft stability regimes.

Near-Surface Stability	Very Shallow Mixed Layer	Stability Above Boundary Layer (“Aloft”)
<b>Near Neutral (NN):</b> $d\theta dz^{-1} < 0.5 K (100 m)^{-1}$	If near-surface stability = NN or WS and ABL height <125 m ➤ Near-surface stability = <b>Very-Shallow Mixed (VSM)</b>	
<b>Weak Stability (WS):</b> $d\theta dz^{-1} \geq 0.5 K (100 m)^{-1}$ and $< 1.75 K (100 m)^{-1}$		<b>Weak Stability Aloft (-WSA):</b> $d\theta dz^{-1} \geq 0.5 K (100 m)^{-1}$ and $< 1.75 K (100 m)^{-1}$
<b>Moderate Stability (MS):</b> $d\theta dz^{-1} \geq 1.75 K (100 m)^{-1}$ and $< 5 K (100 m)^{-1}$		<b>Moderate Stability Aloft (-MSA):</b> $d\theta dz^{-1} \geq 1.75 K (100 m)^{-1}$ and $< 5 K (100 m)^{-1}$
<b>Strong Stability (SS):</b> $d\theta dz^{-1} \geq 5 K (100 m)^{-1}$ and $< 15 K (100 m)^{-1}$		<b>Strong Stability Aloft (-SSA):</b> $d\theta dz^{-1} \geq 5 K (100 m)^{-1}$
<b>Very Strong Stability (VSS):</b> $d\theta dz^{-1} \geq 15 K (100 m)^{-1}$ and $< 30 K (100 m)^{-1}$		<b>Very Strong Stability Aloft (-VSSA):</b> $d\theta dz^{-1} \geq 15 K (100 m)^{-1}$

**Extremely Strong Stability (ESS):**  
 $d\theta dz^{-1} \geq 30 \text{ K (100 m)}^{-1}$

**Extremely Strong Stability Aloft (-ESSA):**  
 $d\theta dz^{-1} \geq 30 \text{ K (100 m)}^{-1}$

294 Regimes where no increased stability aloft is present (NN, WS, MS, SS, VSS, or ESS) as well as  
295 the VSM-WSA will be referred to as “basic near-surface stability regimes”. The reasoning for including  
296 VSM-WSA in the basic near-surface stability regimes is that this regime is defined both by stability as  
297 well as boundary layer depth. The VSM regime is derived from the same conditions that define the NN  
298 and WS regimes, but in the VSM regime, a much shallower boundary layer exists (less than 125 m). The -  
299 WSA in this regime is consistent with the potential temperature gradient that defines the VSM regime as a  
300 whole and is thus considered as part of the basic near-surface stability regimes. Each stability grouping is  
301 identified by a distinct color (Table 3): NN – brown; VSM – red; WS – green; MS – blue; SS – purple;  
302 VSS – pink; ESS – indigo), in which the darkest color is the basic near-surface regime (no increased  
303 stability aloft), and with decreasing color intensity as stability aloft in that regime grouping increases.

304 *Table 3: Boundary Layer Regime acronyms and color codes. On the left is the color and acronym used to*  
 305 *represent*  
 306 *the 20*  
 307 *regimes in*  
 308 *and tables*

<b>Regime Color and Acronym</b>	<b>Regime Full Name</b>
<b>NN</b>	<b>Near Neutral</b>
NN-WSA	Near Neutral- Weak Stability Aloft
NN-MSA	Near Neutral- Moderate Stability Aloft
NN-SSA	Near Neutral- Strong Stability Aloft
<b>VSM-WSA</b>	<b>Very Shallow Mixed- Weak Stability Aloft</b>
VSM-MSA	Very Shallow Mixed- Moderate Stability Aloft
VSM-SSA	Very Shallow Mixed- Strong Stability Aloft
<b>WS</b>	<b>Weak Stability</b>
WS-MSA	Weak Stability- Moderate Stability Aloft
WS-SSA	Weak Stability- Strong Stability Aloft
<b>MS</b>	<b>Moderate Stability</b>
MS-SSA	Moderate Stability- Strong Stability Aloft
<b>MS-VSSA</b>	<b>Moderate Stability- Very Strong Stability Aloft</b>
MS-ESSA	Moderate Stability- Extremely Strong Stability Aloft
<b>SS</b>	<b>Strong Stability</b>
SS-VSSA	Strong Stability- Very Strong Stability Aloft
SS-ESSA	Strong Stability- Extremely Strong Stability Aloft
<b>VSS</b>	<b>Very Strong Stability</b>
VSS-ESSA	Very Strong Stability- Extremely Strong Stability Aloft
<b>ESS</b>	<b>Extremely Strong Stability</b>

*each of stability figures*

309 *throughout this paper, and the full regime name is spelled out on the right. The basic near-surface*  
 310 *stability regimes are denoted in bold font.*

### 311 **2.2.3 Clear and Cloudy Regime Classification**

312 As mentioned in the Introduction, wintertime boundary layer stability in the polar regions is often  
313 described to be made up of two regimes, which differ based on the presence or absence of clouds and the  
314 associated differences in downwelling longwave radiation. This two-regime system is often defined as a  
315 “clear regime” with low values of downwelling longwave radiation, strong surface radiative cooling, and  
316 strong stability, and a “cloudy regime”, with enhanced downwelling longwave radiation, surface warming  
317 and decreased near-surface stability (Phillpot & Zillman, 1970; Stone and Kahl, 1991; Solomon et al.,  
318 2023). Here, we will assess how the frequency of the 20 boundary layer regimes (Table 2) relate to the  
319 more commonly defined clear (strongly stable) and cloudy (weakly stable) regimes to evaluate the use of  
320 this more nuanced view of the relationship between boundary layer stability and cloud cover.

321 To determine the conditions with which the boundary layer regimes defined in Table 2 occur, we  
322 follow the approach of Solomon et al. (2023) that used net longwave radiation observations taken over the  
323 Arctic sea ice during the MOSAiC expedition to define clear and cloudy conditions. They found that  
324 during the winter there was a bimodal distribution of net longwave radiation. The minimum in frequency  
325 between the two peaks of this distribution was used to define clear and cloudy states, which were found to

326 have distinct distributions of downwelling longwave radiation (Solomon et al. 2023). Following Solomon  
327 et al. (2023) this analysis will be completed only in the winter season.

328 PDFs of wintertime net longwave radiation are calculated at the five study sites (Figures S1 to  
329 S5) to determine if bimodal distributions of net longwave radiation are found at coastal and interior  
330 Antarctic sites, like what was found in the Arctic. Then, as in Solomon et al. (2023) we determine if  
331 distinct distributions in downwelling longwave radiation are present, which serve as a proxy for clear  
332 (small values of downwelling longwave radiation) or cloudy (large values of downwelling longwave  
333 radiation) conditions. Solomon et al. (2023) used the minima in the net longwave radiation PDF as a  
334 threshold to define clear and cloudy regimes. In this study, we define an overlap ratio (defined below) that  
335 quantifies how distinct the distributions of downwelling longwave radiation are for a given net longwave  
336 radiation threshold used to separate clear and cloudy states. For the identified net longwave radiation  
337 threshold, we create two PDFs of downwelling longwave radiation (Figures S1 to S5) based on the subset  
338 of observations corresponding to net longwave radiation values above (cloudy) or below (clear) the net  
339 longwave radiation threshold. Using the two downwelling longwave radiation PDFs, we determine the  
340 total number of clear cases, cloudy cases, and the number of coincident cases where the clear and cloudy  
341 PDFs overlap. The overlap ratio is calculated as the number of overlapping cases divided by the total  
342 number of clear and the total number of cloudy cases, and the final overlap ratio is the maximum of these  
343 two ratios. This overlap ratio quantifies how much overlap exists between the clear and cloudy  
344 downwelling longwave radiation PDFs and distinct clear and cloudy PDFs are characterized by low  
345 overlap ratios. The overlap ratio is calculated for each value of net longwave radiation (from the  
346 minimum to the maximum observed), at  $1 \text{ W m}^{-2}$  intervals, at each site. The minimum overlap ratio at  
347 each site, from the calculations every  $1 \text{ W m}^{-2}$ , defines the net longwave radiation threshold identifying  
348 the most distinct distributions of downwelling longwave radiation for clear and cloudy cases. It generally  
349 corresponds to within a few  $\text{W m}^{-2}$  of the minimum in bimodal PDF of net longwave radiation (vertical  
350 black line in Figures S1 to S5). The dates and times corresponding to the clear and cloudy states were  
351 used to determine the frequency of boundary layer stability regimes for the two states.

### 352 **3 Results**

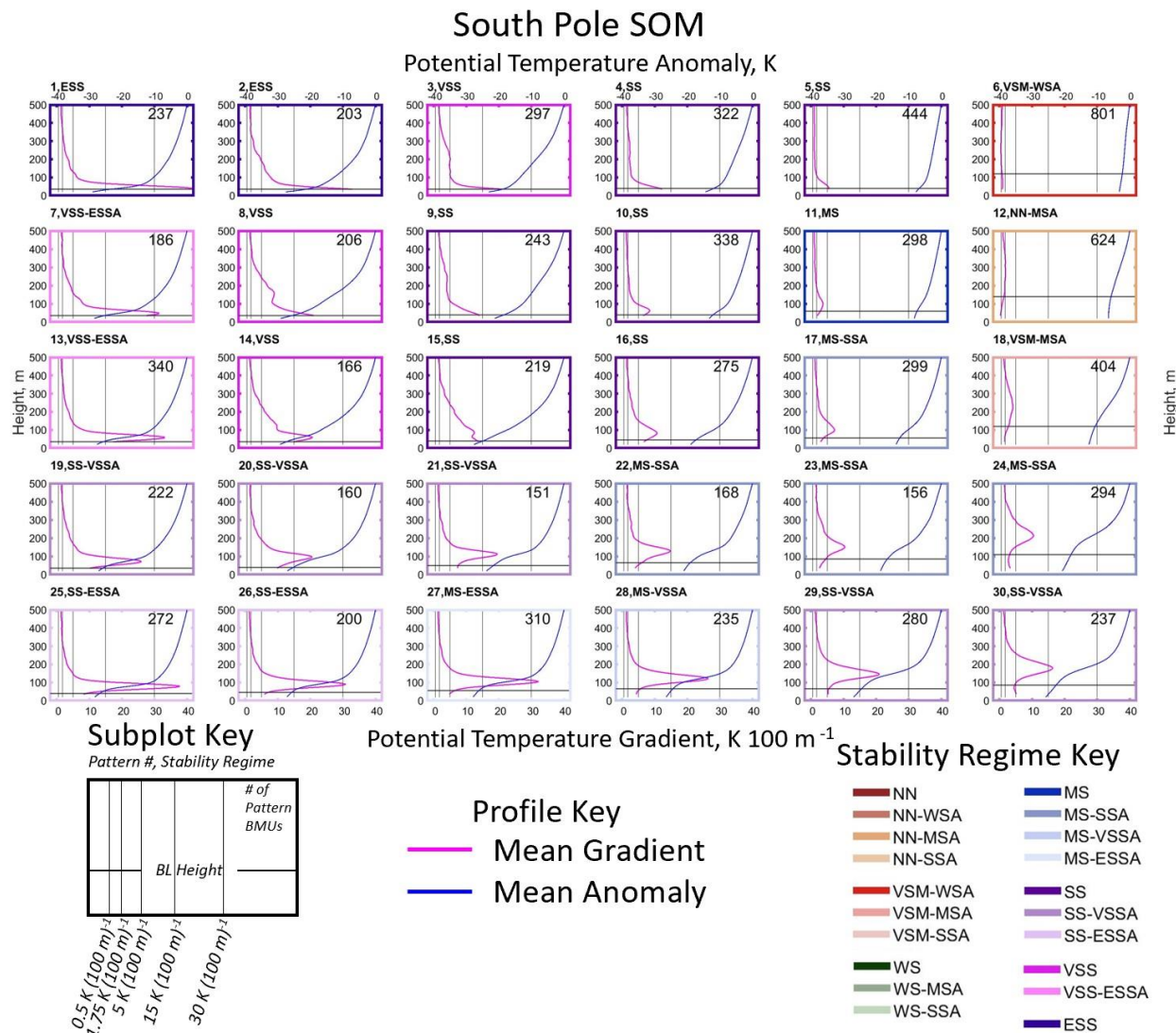
#### 353 **3.1 South Pole**

354 At a high-plateau, continental interior site such as South Pole, it is expected that strong stability  
355 will be present throughout much of the year (Phillpot and Zillman, 1970; Comiso, 1994; Hudson and  
356 Brandt, 2005; Zhang, et al., 2011). The SOM in Figure 2 shows the range of potential temperature  
357 profiles (anomaly and gradient) across 16 years of radiosonde observations at South Pole, as well as the  
358 stability regime (colored outline and label in top left of each pattern) corresponding to the mean profiles  
359 in each SOM pattern. The left side of the SOM is dominated by the strongest stability patterns, and  
360 stability decreases from left to right, with the weakest stability patterns in the upper right corner. Potential  
361 temperature gradients more than  $5 \text{ K (100 m)}^{-1}$  in nearly all of the SOM-identified patterns in Figure 2,  
362 with many greater than  $15 \text{ K (100 m)}^{-1}$ , and some even greater than  $30 \text{ K (100 m)}^{-1}$ , shows that strong  
363 stability is in fact common at this site. Potential temperature gradients in excess of  $15 \text{ K (100 m)}^{-1}$ ,  
364 corresponding to our VSS regime (Table 2), are rarely observed outside of the interior of Antarctica, or  
365 over the Greenland ice sheet or Siberia in the Arctic (Zhang et al., 2011). Potential temperature gradients  
366 less than  $1.75 \text{ K (100 m)}^{-1}$ , corresponding to NN or WS regimes, occur only in patterns 6, 12, and 18 in  
367 the upper right of the SOM, emphasizing the dominance of strong stability at South Pole.

368 The height of the maximum potential temperature gradient within the profile varies across the  
369 SOM, often being located very close to the surface, as in the top left corner of the SOM, but sometimes

370 the maximum gradient is located above a layer of decreased stability near the surface, as is in the bottom  
 371 two rows of the SOM. These SOM patterns represent conditions with moderate or strong near-surface  
 372 stability capped by enhanced stability aloft (-SSA, -VSSA, or -ESSA).

373 The SOM for South Pole (Figure 2) shows the boundary layer height for each SOM pattern, in  
 374 addition to showing potential temperature gradient and anomaly profiles. The boundary layer depth rarely  
 375 exceeds 100 m across the SOM and is very shallow (less than 50 m AGL) for the SS, VSS, and ESS cases  
 376 present throughout much of the SOM. Boundary layer depth increases in the MS cases in the bottom right  
 377 corner of the SOM (approximately 100 m) and is deepest in the NN and VSM cases in the top right of the  
 378 SOM (just above 100 m).

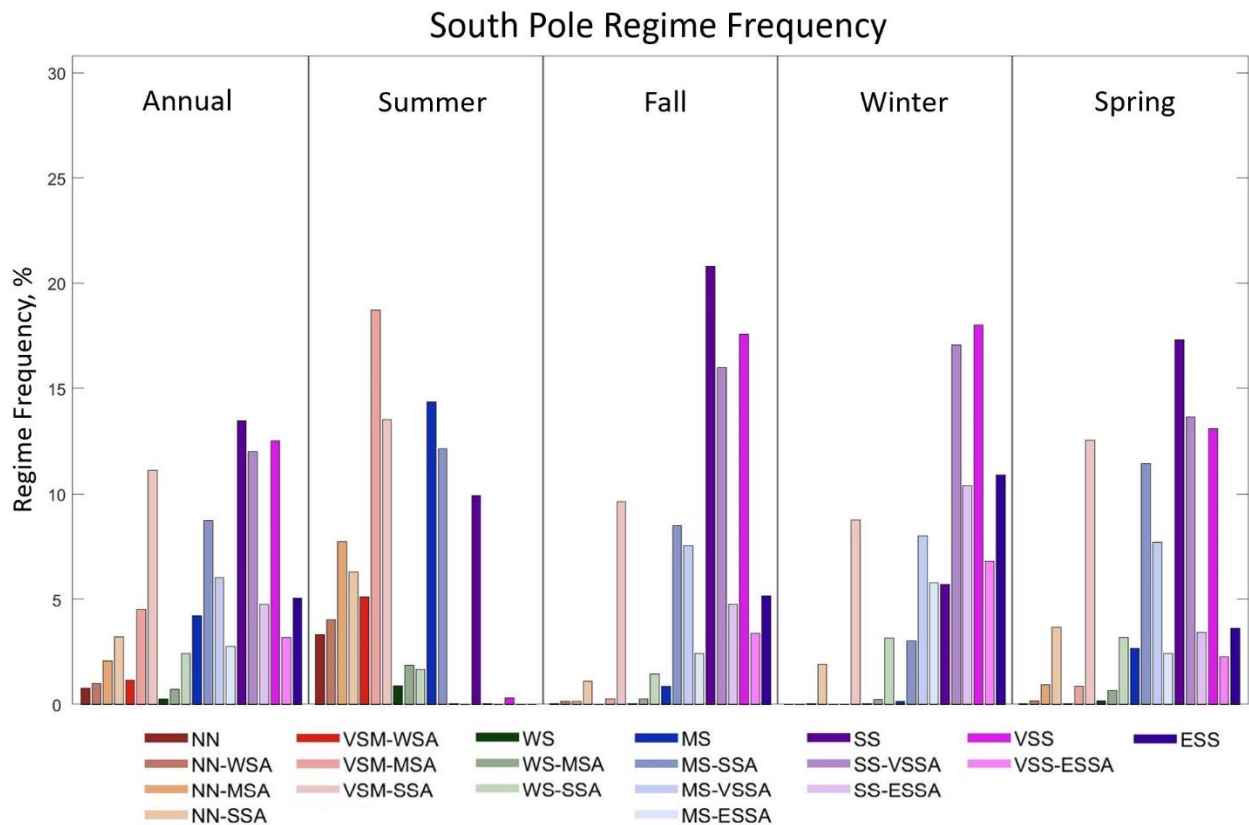


379 Figure 2: Profiles of mean potential temperature gradient (pink line, bottom axis), and mean potential temperature  
 380 anomaly (blue line, top axis) calculated from the BMUs that map to each SOM pattern from 20 to 500 m above  
 381 ground level at South Pole.

382 As mentioned in Section 2.2.2, the stability regime for each individual radiosonde profile was  
 383 identified to allow for comparison of regime frequencies across all five sites. Annual and seasonal  
 384 stability regime frequencies at South Pole are shown in Figure 3. When analyzing the frequency of

385 boundary layer stability regimes on an annual basis (Figure 3, left panel) the strongest near-surface  
 386 stability regimes (SS, VSS and ESS) are most common, occurring 58.5% of the time cumulatively. This  
 387 observation is consistent with what is seen in the SOM, where most of the profiles are SS, VSS, and ESS  
 388 regimes. For the weaker stability regimes (NN, VSM, and WS) the most common types of these regimes  
 389 are the ones with enhanced stability aloft indicating that most of the time when weak stability is present  
 390 near the surface moderate or strong stability remains aloft. Regardless of where strong stability occurs in  
 391 the profile (near-surface or aloft), strong stability, very strong stability, and extremely strong stability  
 392 occurs 85.1% of the time annually at the South Pole indicating that this location is dominated by the  
 393 strongest stability classes.

394 Seasonally there is a clear difference in regime frequencies between summer (DJ) and the other  
 395 three seasons. In the summer, the weakest near-surface stability regimes (NN and VSM) account for most  
 396 summer cases (58.7%), although often with enhanced stability aloft. Despite the sun being continuously  
 397 above the horizon during the summer, a high frequency of the MS and SS regimes (36.8%) still occurs.  
 398 WS regimes are very rare (4.5%), along with the VSS and ESS regimes, which almost never occur at this  
 399 time of year. In the winter (MJJA), SS, VSS, and ESS regimes dominate, occurring 68.9% of the time,  
 400 while NN and VSM occur only 10.7% of time, and WS and MS cases make up the remainder of stability  
 401 regimes observed in winter (3.4% and 16.9%, respectively). Interestingly, the few NN, VSM, and WS  
 402 cases in the winter all have strong stability aloft (-SSA), indicating that even when the weakest stability  
 403 regimes occur at the surface, strong stability is still present just above the boundary layer. The frequency  
 404 of stability regimes in the transition seasons (fall, FMA, and spring, SON) largely mirrors the frequency  
 405 of stability regimes in winter, again with the observation that the NN, VSM, and WS cases in the fall and  
 406 spring almost always have strong stability aloft (-SSA).





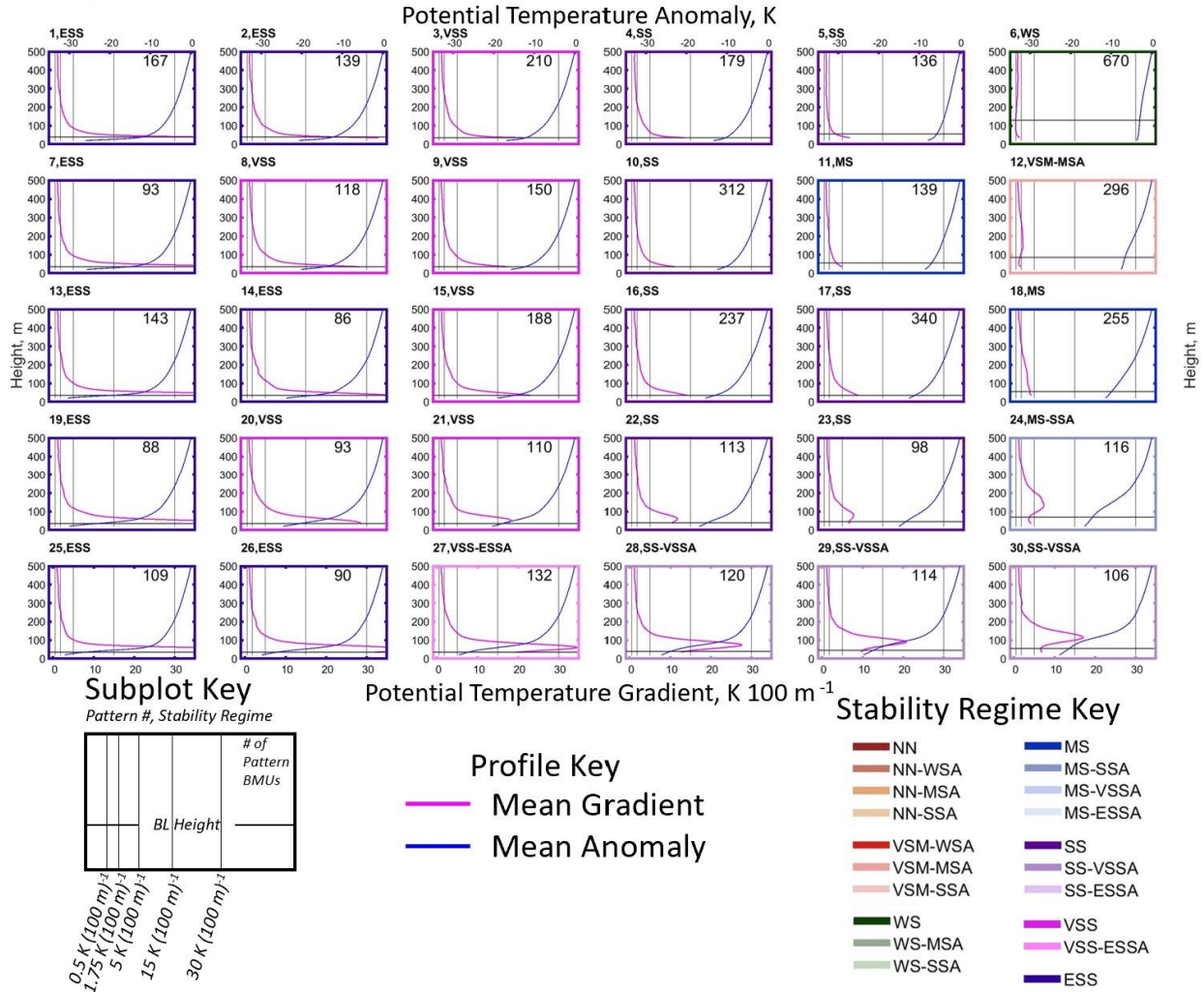
407 *Figure 3: Percentage of observations corresponding to each boundary layer stability regime observed at South Pole*  
408 *annually (left panel) and seasonally (right 4 panels - summer, fall, winter, and spring). The regimes for the annual*  
409 *and seasonal plots are arranged with increasing stability from left to right in each panel, and the order of the*  
410 *stability regimes in each panel corresponds to the order of the regimes, from top to bottom and left to right in the*  
411 *colored key at the bottom.*

### 412 **3.2 Dome C**

413 Dome C is another high-plateau continental interior site where strong stability persists throughout  
414 much of the year (King and Turner, 1997; Andreas et al., 2000). This can be seen in the Dome C SOM in  
415 Figure 4, where, like South Pole, most of the SOM-identified profiles exhibit potential temperature  
416 gradients in excess of  $5 \text{ K (100 m)}^{-1}$ , and many are greater than  $15 \text{ K (100 m)}^{-1}$ . The left four columns of  
417 the SOM are all SS or stronger stability regimes (greater than  $5 \text{ K (100 m)}^{-1}$ ), and stability decreases from  
418 left to right with the weakest stability patterns in the upper right corner (less than  $1.75 \text{ K (100 m)}^{-1}$ ). The  
419 height of the maximum potential temperature gradient within the profile changes across the SOM, with  
420 the maximum stability observed at the surface in the upper left profiles, and the height of this maximum  
421 stability increasing to the bottom right of the SOM, although the strongest stability usually occurs near the  
422 surface in most of the SOM patterns.

423 The boundary layer height is less than 50 m across most of the SOM, and only increases when  
424 stability decreases, such as in the bottom right, where stability is moderate and the boundary layer height  
425 is about 75 m, and in the top right, where stability is weak, and the boundary layer height is around 100  
426 m. In general, these are still very shallow boundary layers, even in the weaker stability patterns, compared  
427 to other locations across the planet, where the height of the boundary layer can exceed 1000 m (Stull,  
428 1988). Both at South Pole and Dome C strong, near-surface stability suppresses most of the mechanically  
429 generated turbulence resulting in very shallow (typically less than 75 m) boundary layers. However,  
430 shallow boundary layers at both sites also occur in the upper right portions of the SOM where relatively  
431 weak stability exists, indicating that near-surface turbulent mixing is still confined to the lowest part of  
432 the atmosphere (less than 150 m).

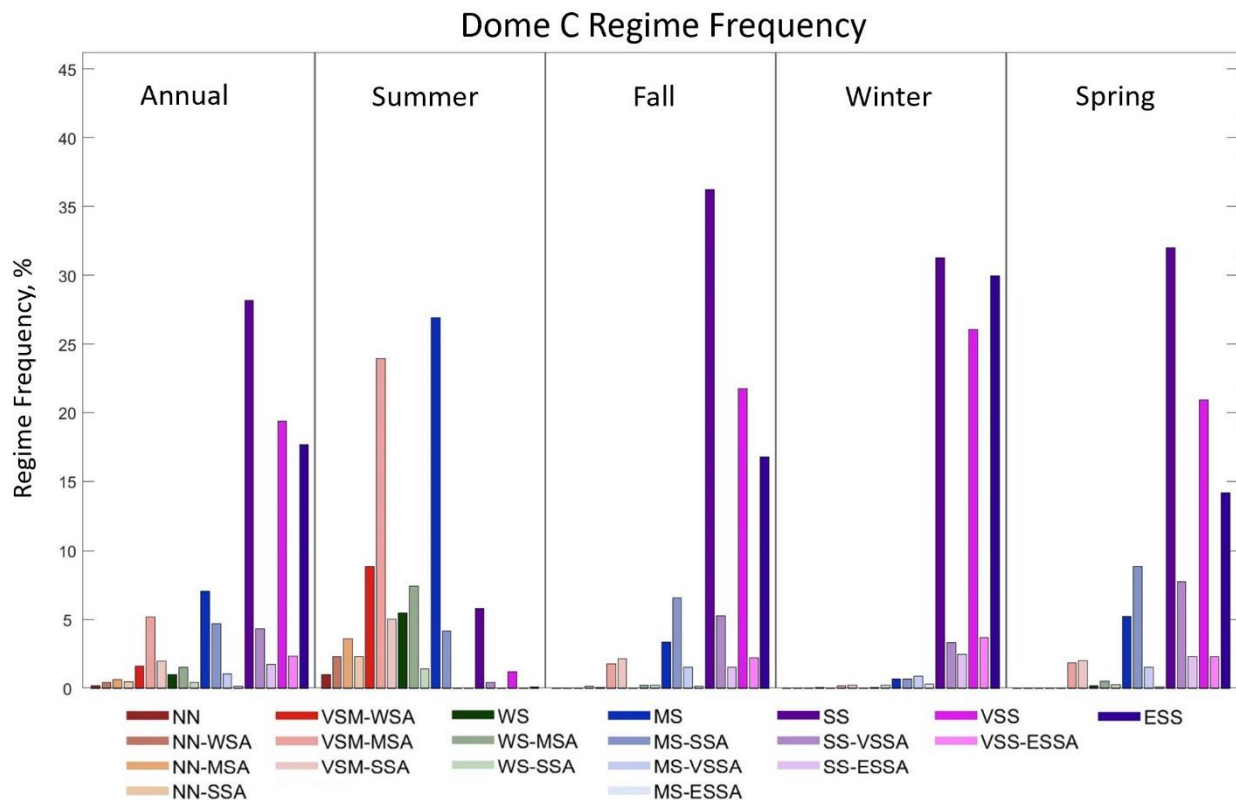
# Dome C SOM



433 Figure 4: Profiles of mean potential temperature gradient (pink line, bottom axis), and mean potential temperature  
 434 anomaly (blue line, top axis) calculated from the BMUs that map to each SOM pattern from 20 to 500 m above  
 435 ground level at Dome C.

436 The frequency of occurrence of each stability regime at Dome C is shown in Figure 5. On an  
 437 annual basis, SS, VSS and ESS regimes occur most frequently (73.6%), while the weaker stability  
 438 regimes, NN, VSM, and WS only occur 13.5%. This is comparable to the range of stability regimes seen  
 439 in the SOM, where these types of weaker stability regimes occur very rarely, and SS, VSS, and ESS  
 440 regimes dominate across most of the SOM. A strong seasonal cycle emerges, with the weaker stability  
 441 regimes dominant in summer and the strongest stability regimes dominant in winter. The summer season  
 442 is largely characterized by NN, VSM, and WS regimes (61.4%), as well as MS regimes (31.1%). In the  
 443 summer, SS, VSS, and ESS regimes occur only 7.5% of the time, indicating the rarity of strong stability  
 444 at this time of year. In the winter, SS, VSS, and ESS regimes occur almost exclusively (96.7%), while all  
 445 the other regime groupings (VSM, NN, WS, and MS) occur very rarely (3.3%). It is also interesting that  
 446 the dominant regimes in the winter are solely the basic near-surface stability regimes of SS, VSS, and  
 447 ESS regimes, and increased stability aloft in these regimes occurs much less frequently indicating that  
 448 during the winter the strongest stability occurs at the surface most of the time, with infrequent cases of  
 449 weakened stability near the surface and enhanced stability aloft. The frequency of stability regimes in the

450 transition seasons (fall and spring) is also dominated by stronger stability regimes (SS, VSS and ESS),  
 451 although with slightly lower frequencies than in winter, with these regimes occurring 83.7% and 76.9% of  
 452 the time in fall and spring respectively. The weakest stability regimes (VSM, NN, and WS) occur rarely  
 453 (4.6% and 4.9% of the time in fall and spring, respectively), while the MS regime occurs 11.7% and  
 454 15.7% of the time in fall and spring, respectively. In comparison to the summer and winter, the transition  
 455 seasons behave more like the winter season when it comes to regime frequency, with most regimes being  
 456 strong stability.



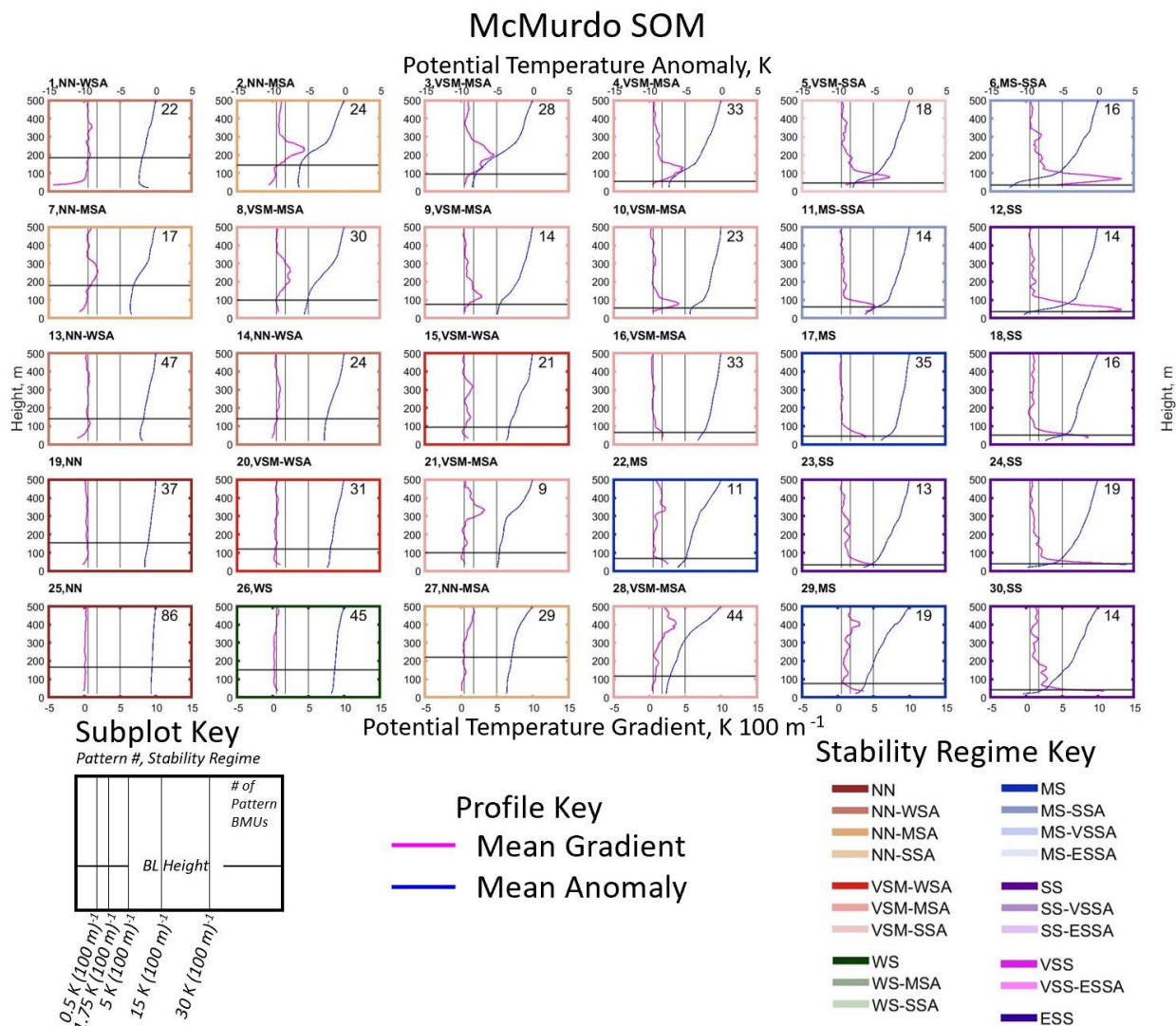
457 *Figure 5: Percentage of observations corresponding to each boundary layer stability regime observed at Dome C*  
 458 *annually (left panel) and seasonally (right 4 panels - summer, fall, winter, and spring). The regimes for the annual*  
 459 *and seasonal plots are arranged with increasing stability from left to right in each panel, and the order of the*  
 460 *stability regimes in each panel corresponds to the order of the regimes, from top to bottom and left to right in the*  
 461 *colored key at the bottom.*

### 462 3.3 McMurdo

463 So far, two continental interior sites, South Pole and Dome C have been analyzed, and now the  
 464 coastal sites, McMurdo, Neumayer, and Syowa will be analyzed. In comparison to the continental  
 465 interior, coastal locations are more exposed to the impacts of cyclonic activity, increased cloud cover and  
 466 moisture, as well as warmer surface temperatures and weaker inversions (Phillpot and Zillman, 1970;  
 467 Cassano et al., 2016). Given these previous observations, it is expected that weaker stability will be  
 468 present at the coastal sites compared to the near-constant state of strong stability observed at the colder,  
 469 continental interior sites described above.

470 Stability profiles at McMurdo identified by the SOM span a range from NN to SS regimes, as  
 471 seen in Figure 6. Stability in the SOM increases from left to right, with the weakest stability patterns in

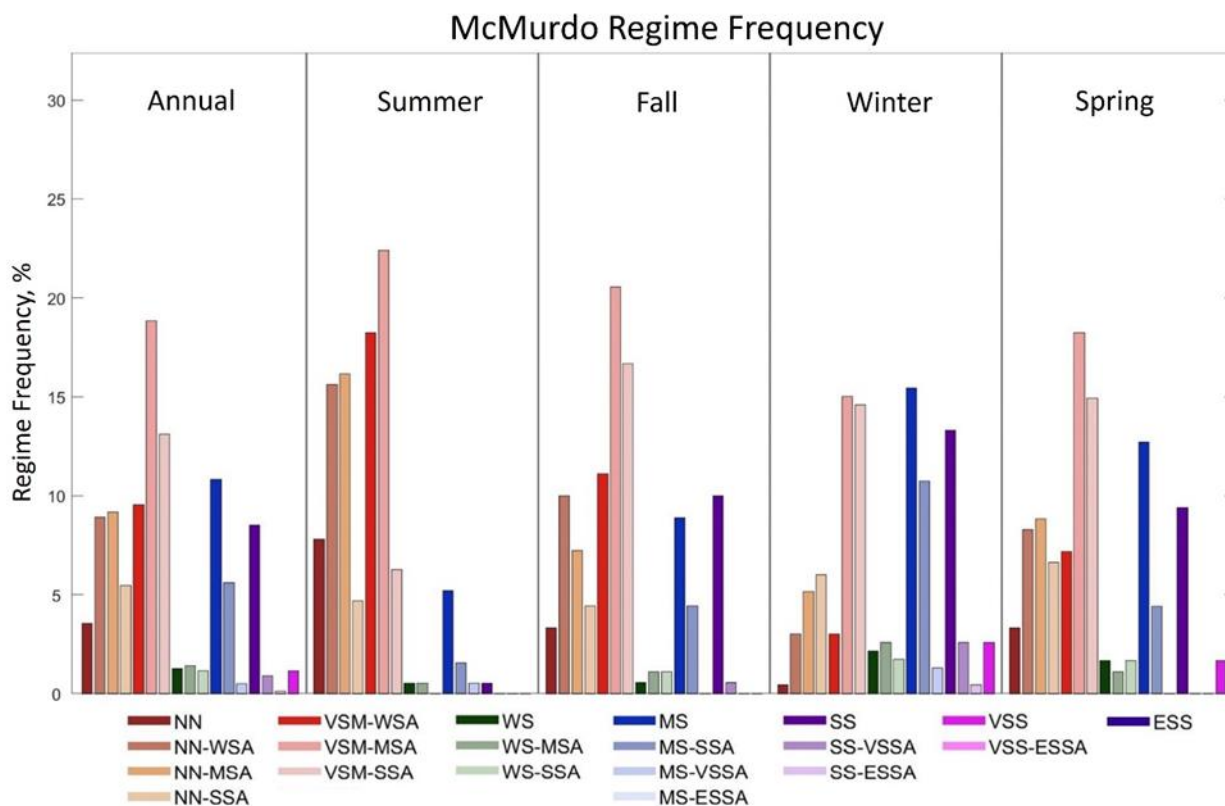
472 the top left and strongest stability patterns in the bottom right. In addition to this gradient in stability  
 473 across the SOM the height of the strongest stability increases from the surface in the bottom rows of the  
 474 SOM to above a near surface layer of weaker stability in the top middle of the SOM. Most of these  
 475 patterns with enhanced stability aloft exhibit moderate or strong stability (-MSA or -SSA, respectively)  
 476 above a layer of weaker stability. Two-thirds of the SOM patterns exhibit potential temperature gradients  
 477 less than  $1.75 \text{ K (100 m)}^{-1}$ , corresponding to WS or weaker stability, and only five patterns on the right  
 478 side of the SOM (patterns 12, 18, 23, 24, and 30) exhibit strong stability with gradients greater than  $5 \text{ K}$   
 479  $(100 \text{ m})^{-1}$ . It can also be seen that the height of the boundary layer increases from the bottom right  
 480 (approximately 50 m) to the top left (approximately 200 m), as stability decreases, and the height of the  
 481 maximum stability increases in the profile.



482 *Figure 6: Profiles of mean potential temperature gradient (pink line, bottom axis), and mean potential temperature*  
 483 *anomaly (blue line, top axis) calculated from the BMUs that map to each SOM pattern from 20 to 500 m above*  
 484 *ground level at McMurdo.*

485 Considering regime frequencies on an annual basis the NN and VSM regimes are most common  
 486 (68.6 %), followed by MS and SS regimes (24.9 %). The summer season is dominated by NN and VSM  
 487 regimes (91.2%), and WS, MS, and SS regimes occur only 8.8% of the time. This distribution of stability

488 is consistent with increased radiative forcing and previous observations of weaker stability in summer  
 489 compared to other seasons at a site approximately 100 km from McMurdo (Cassano et al., 2016). In the  
 490 winter, when it would be expected that strong stability would be dominant, only about half of the time  
 491 regimes with stability MS and greater occur (46.4%) while regimes with stability WS and weaker occur  
 492 just over half of the time (53.6%). However, when the regimes with stability WS and weaker occur,  
 493 moderate or strong stability aloft (-MSA and -SSA, respectively) is usually present (84% of NN, VSM,  
 494 and WS cases have -MSA or -SSA), indicating that even when weaker stability occurs near the surface  
 495 moderate or stronger stability is present just above the boundary layer. In the transition seasons, MS and  
 496 stronger cases occur 23.9% of the time in the fall and 28.2% of the time in the spring. NN and VSM cases  
 497 cumulatively occur 73.3% of the time in fall and 67.3% in the spring, while WS cases are largely absent.  
 498 In the VSM regime grouping, the -MSA and -SSA regimes are most common with the -WSA regime  
 499 occurring less frequently in comparison in both spring and fall. In the NN regime grouping, the frequency  
 500 of occurrence decreases with increasing stability aloft in the fall, and is more consistent across the -WSA,  
 501 -MSA, and -SSA regimes in the spring. This indicates that in the fall, it is more common for NN cases to  
 502 have weak rather than strong stability aloft, like what was observed in the summer, and opposite that in  
 503 the winter.

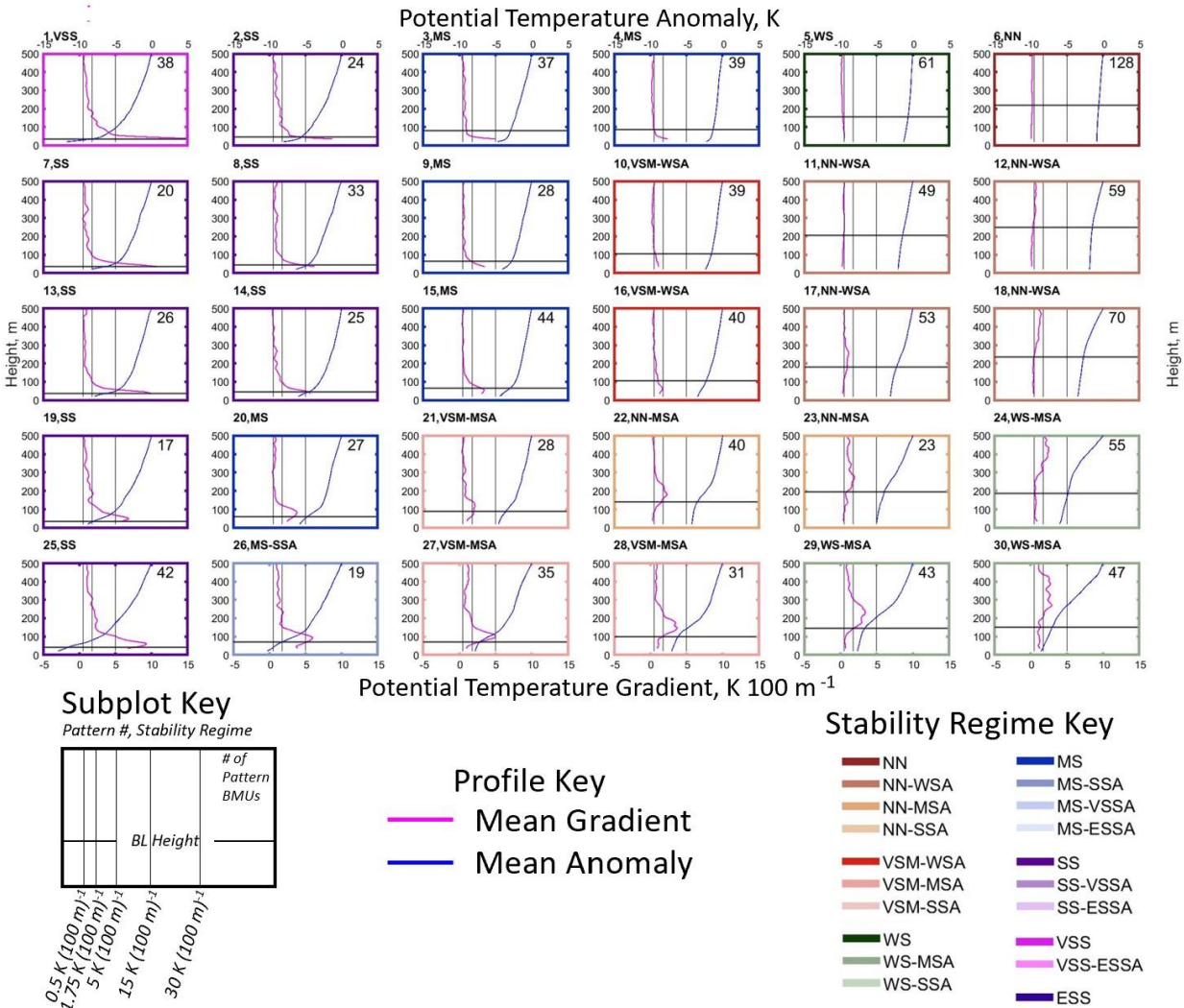


504 *Figure 7: Percentage of observations corresponding to each boundary layer stability regime observed at McMurdo*  
 505 *annually (left panel) and seasonally (right 4 panels - summer, fall, winter, and spring). The regimes for the annual*  
 506 *and seasonal plots are arranged with increasing stability from left to right in each panel, and the order of the*  
 507 *stability regimes in each panel corresponds to the order of the regimes, from top to bottom and left to right in the*  
 508 *colored key at the bottom.*

### 509 3.4 Neumayer

510 Neumayer is a coastal site located near sea-level, heavily influenced by large-scale cyclonic  
511 activity (Silva et al., 2022), and where the proximity of sea ice and open ocean can affect boundary layer  
512 stability throughout the year (Silva et al., 2022). Stability regimes at Neumayer span a range from NN to  
513 VSS regimes, as seen in the SOM in Figure 8. Generally, stability decreases from left to right across the  
514 SOM. Stability on the left side of the SOM decreases from the top to the bottom of the SOM, with the  
515 strongest stability regimes in the top left. On the right side of the SOM deep near neutral or weak stability  
516 patterns occur at the top of the SOM with patterns characterized by increasing stability aloft occurring  
517 towards the bottom of the SOM. This SOM shows two general modes of stability split by a bottom left to  
518 top right diagonal, with the portion to the right of this diagonal characterized by NN, VSM, and WS  
519 regimes, and the portion to the left characterized by MS, SS, and VSS regimes. The boundary layer height  
520 at Neumayer increases from the left side of the SOM, where very shallow boundary layers exist (less than  
521 50 m) with strong stability, to the top right, where the boundary layer height increases to above 200 m.

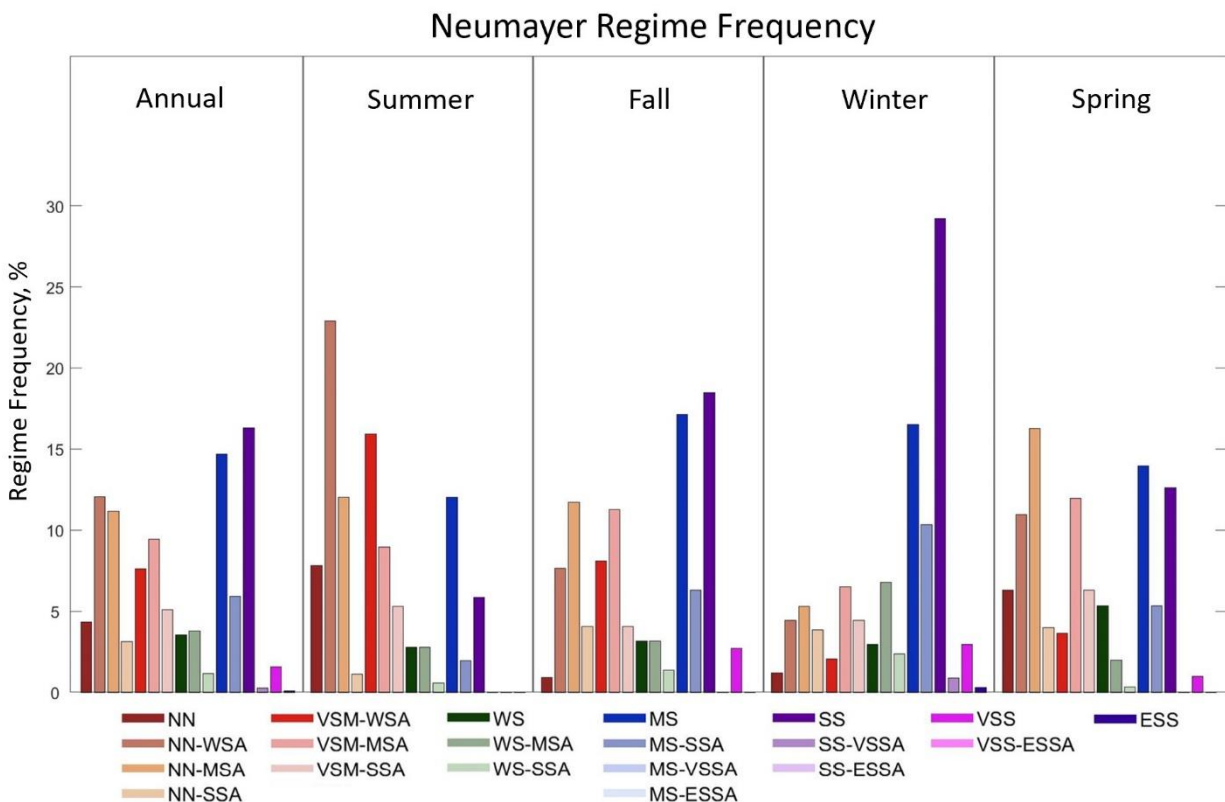
# Neumayer SOM



522 Figure 8: Profiles of mean potential temperature gradient (pink line, bottom axis), and mean potential temperature  
 523 anomaly (blue line, top axis) calculated from the BMUs that map to each SOM pattern from 20 to 500 m above  
 524 ground level at Neumayer.

525 On an annual basis, the NN and VSM regime groupings are most common (52.8%), and the MS  
 526 and SS (37.2%) regimes occur slightly less frequently at Neumayer (Figure 9). The WS regime grouping  
 527 occurs 8.4% while VSS and ESS regimes are rare and occur only 1.6% of the time throughout the year.  
 528 The summer season is dominated by NN and VSM regimes (74%). WS (6.1%), MS (14%), and SS  
 529 (5.9%) regimes are much less common in comparison. In the VSM and NN regime groupings regimes  
 530 with weak stability aloft (-WSA) are more common than those with stronger stability aloft (-MSA and -  
 531 SSA). In the winter, regimes with MS or greater stability are most common (60.1%), while regimes with  
 532 weaker stability, WS (12.2%), VSM (13%), and NN (14.7%), occur less frequently. Further, many of the  
 533 weaker stability regimes present in the winter are those with increased stability aloft, especially -MSA  
 534 and -SSA, indicating that moderate or stronger stability is frequently present either near the surface or  
 535 aloft in winter (89.5% of the time), whereas in the summer these moderate or strong stability cases (either  
 536 at the surface or aloft) cumulatively occur 50.7% of the time. In the fall, NN and VSM cases (47.9%) and  
 537 MS and stronger cases (44.6%) occur with almost equal frequency, unlike in the summer when the NN

538 and VSM cases are dominant, and winter when the MS and stronger cases are dominant. In the spring, the  
 539 VSM and NN cases (59.6%) occur more frequently than the MS and stronger cases (32.9%), which is  
 540 more similar to the distribution of regimes in the summer, when weaker stability regimes dominate.



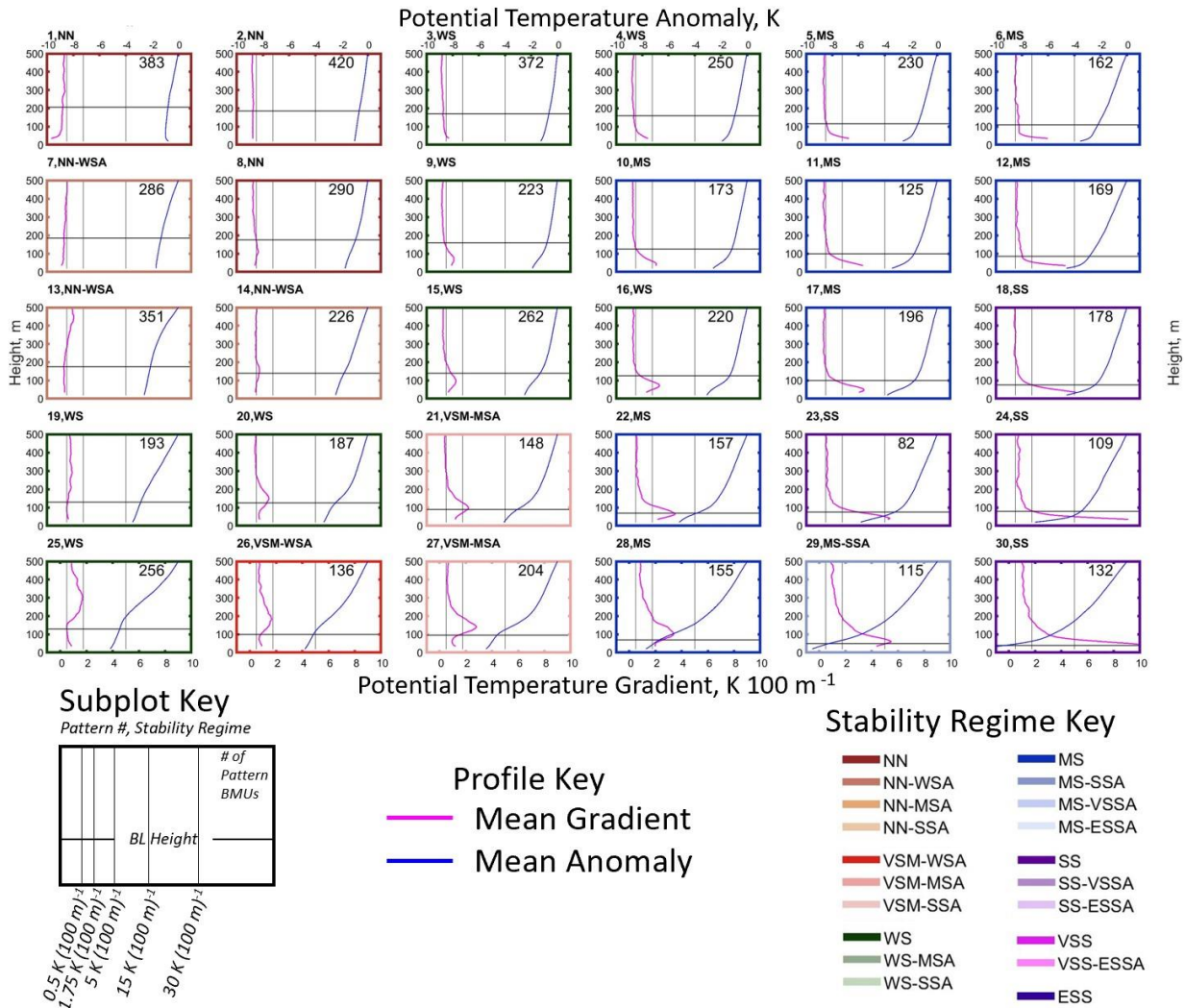
541 *Figure 9: Percentage of observations corresponding to each boundary layer stability regime observed at Neumayer*  
 542 *annually (left panel) and seasonally (right 4 panels - summer, fall, winter, and spring). The regimes for the annual*  
 543 *and seasonal plots are arranged with increasing stability from left to right in each panel, and the order of the*  
 544 *stability regimes in each panel corresponds to the order of the regimes, from top to bottom and left to right in the*  
 545 *colored key at the bottom.*

### 546 3.5 Syowa

547 Syowa is a coastal site near sea-level, impacted cyclonic activity and by katabatic winds from the  
 548 continental interior (Murakoshi, 1958), which sometimes result in strong wind events (Yamada and  
 549 Hirasawa, 2018). Stability at Syowa spans a range from NN (top left corner of SOM) to SS (bottom right  
 550 corner of SOM) regimes, as seen in the SOM in Figure 10. Stability generally increases from left to right  
 551 and top to bottom across the SOM. The height of the maximum potential temperature gradient is near the  
 552 surface on the far-right side of the SOM and increases to approximately 300 m in the bottom left. Shallow  
 553 boundary layers associated with the strong stability patterns in the bottom right increase in height to the  
 554 top left, where near neutral conditions extend through a deeper, 200 m boundary layer.



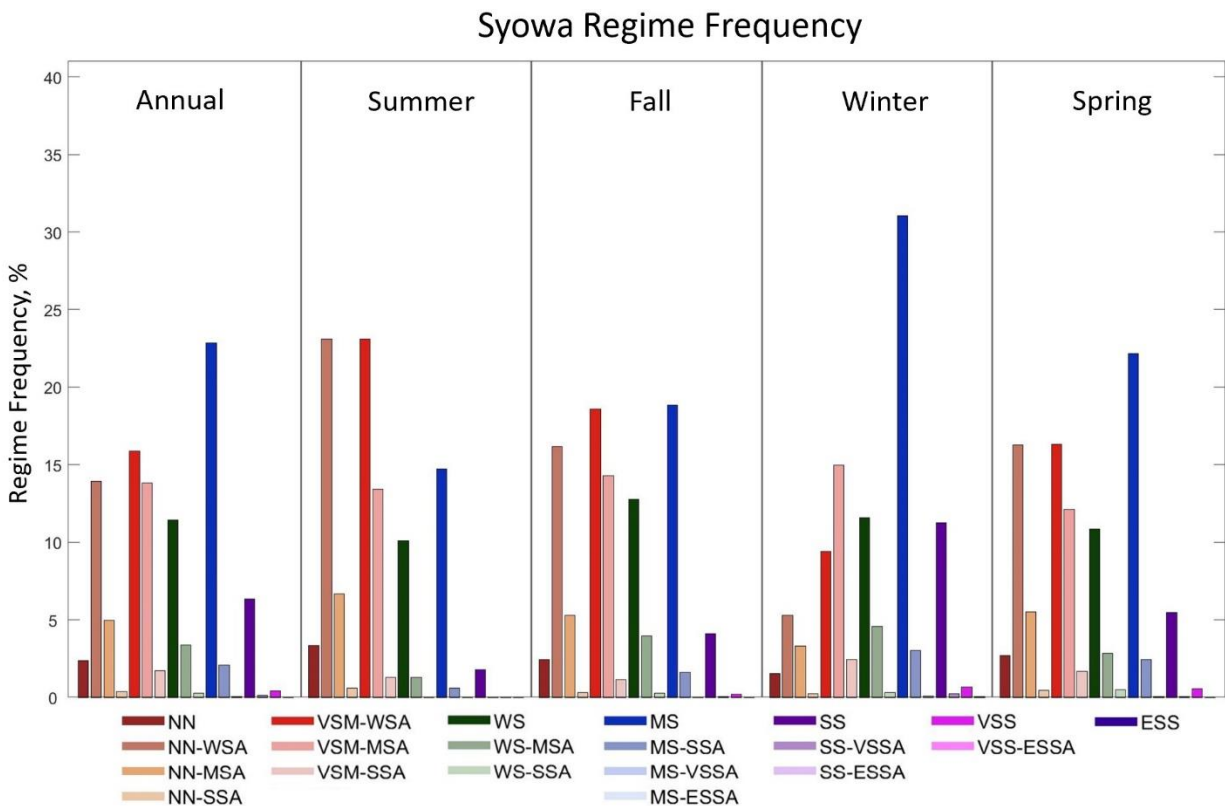
# Syowa SOM



555 Figure 10: Profiles of mean potential temperature gradient (pink line, bottom axis), and mean potential temperature  
 556 anomaly (blue line, top axis) calculated from the BMUs that map to each SOM pattern from 20 to 500 m above  
 557 ground level at Syowa.

558 The frequency of occurrence of each stability regime at Syowa, annually and seasonally, is shown  
 559 in Figure 11. On an annual basis, a mix of regimes are observed, mostly in the NN (21.8%) and VSM  
 560 (31.4%) regime groupings, with enhanced stability aloft common. The WS regime (15.1%) and MS  
 561 regime (25.1%) also occur frequently, on an annual basis, but enhanced stability aloft rarely occurs in  
 562 these regime groupings. The strongest stability regimes (SS, VSS and ESS) occur infrequently (6.8%).  
 563 These results indicate that near neutral to moderate stability is most common at Syowa, while stronger  
 564 stability is rare. The summer season is dominated by the NN and VSM regimes (71.5%), while the WS  
 565 regime occurs 11.4% of the time, and the MS regime 15.3% of the time. In all regime groupings in the  
 566 summer, strong stability aloft (-SSA) regimes are less common than weak or moderate stability aloft (-  
 567 WSA and -MSA, respectively), which is reflective of the lack of strong stability regimes in general in this  
 568 season. In the winter, MS and SS regimes (45.4%) occur about as often as the NN and WS regimes  
 569 (43.4%), but MS is by far the most common individual regime in winter (31%). Regimes with increased  
 570 stability aloft (-MSA and -SSA) are uncommon in the winter except in the VSM regime grouping, and

571 rather the basic near-surface stability regimes (without enhanced stability aloft) or -WSA cases are more  
 572 common. In the transition seasons, a variety of regimes occur with similar frequencies. In the fall the most  
 573 common regime groupings are the VSM cases (34%) followed by the NN cases (24.2%) and the MS cases  
 574 (20.4%), and in the spring, the VSM (30.5%) regimes are most common followed by MS (24.6%), and  
 575 NN (24.5%) regimes that occur with nearly identical frequencies. In both seasons, like the summer and  
 576 winter, -MSA and -SSA cases occur rarely, with -WSA being more common when increased stability  
 577 aloft is observed for a given regime grouping.



578 *Figure 11: Percentage of observations corresponding to each boundary layer stability regime observed at Syowa*  
 579 *annually (left panel) and seasonally (right 4 panels - summer, fall, winter, and spring). The regimes for the annual*  
 580 *and seasonal plots are arranged with increasing stability from left to right in each panel, and the order of the*  
 581 *stability regimes in each panel corresponds to the order of the regimes, from top to bottom and left to right in the*  
 582 *colored key at the bottom.*

### 583 3.6 Stability Regime Frequencies for Clear and Cloudy Conditions

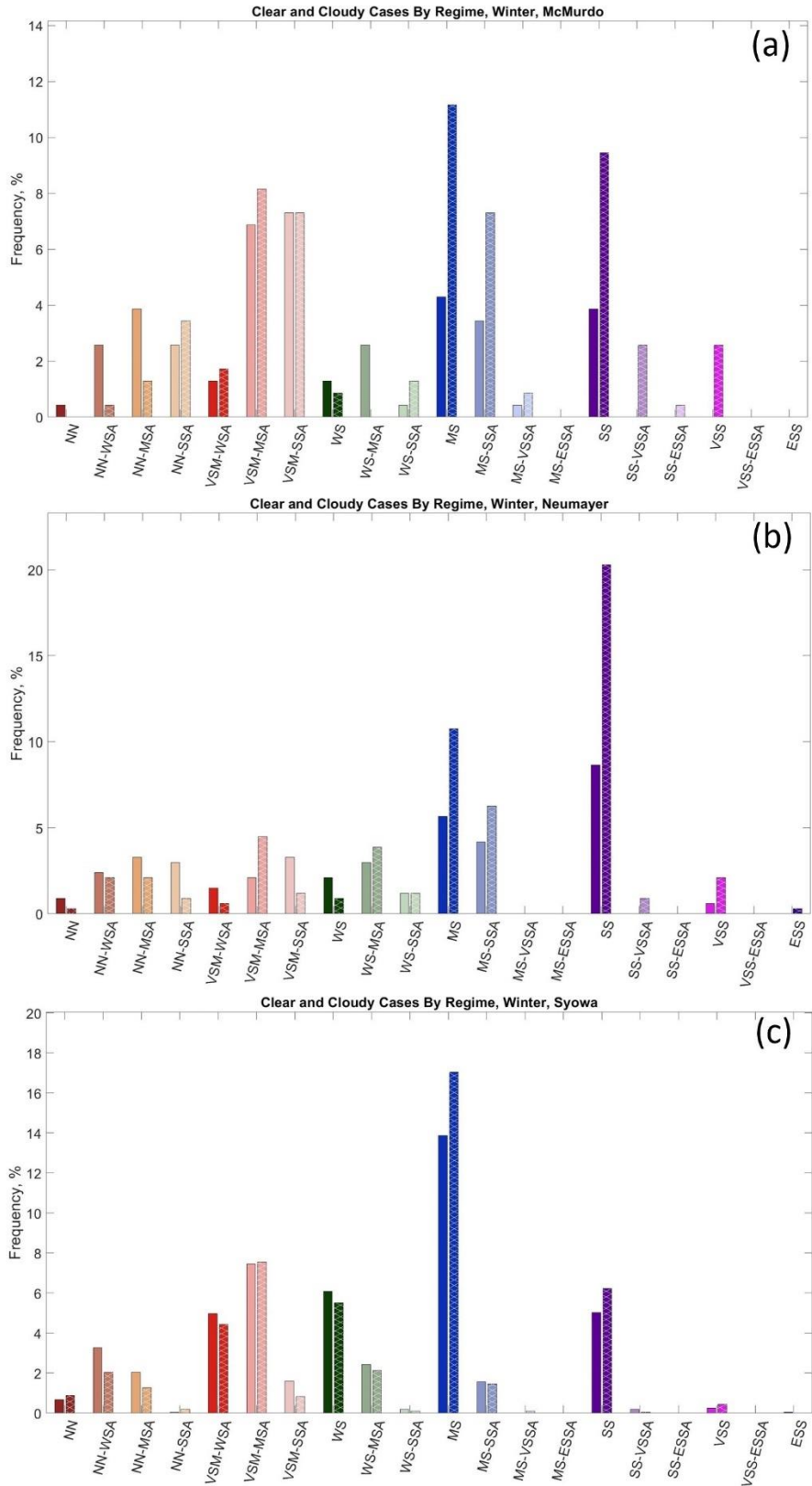
584 As discussed in the introduction and methods, stability in the polar boundary layer is often  
 585 described in the literature as a two-regime system, with cloudy states characterized by large values of  
 586 downwelling longwave radiation and weak stability and clear states characterized by small values of  
 587 downwelling longwave radiation and strong stability (Mahrt et al., 1998; Mahrt, 2014; Solomon et al.,  
 588 2023). To determine if this two-regime description of boundary layer stability and cloud cover is observed  
 589 in the Antarctic a clear or cloudy attribution was given to each radiosonde profile based on the surface net  
 590 longwave radiation value at the time of launch following the method described in Section 2.2.3, based on  
 591 Solomon et al. (2023).

592 Solomon et al. (2023) found that the difference between cloudy and clear states in the Arctic  
593 could be defined by a threshold value of net longwave radiation marking the minimum in the PDF  
594 between two peaks in a bimodal distribution of net longwave radiation. PDFs of winter net longwave  
595 radiation at the five Antarctic sites analyzed in this paper are shown in Figures S1 to S5. The PDFs for the  
596 two interior sites (Dome C and South Pole, Figures S1 and S2) do not show a bimodal distribution while  
597 the three coastal sites do (Figures S3 to S5). The overlap ratio for the cloudy and clear downwelling  
598 longwave radiation PDFs for each site, as described in Section 2.2.3, further support the lack of distinct  
599 cloudy and clear radiative states at the interior sites, with large values of this ratio (0.84 at South Pole and  
600 0.91 at Dome C) indicating that there is no value of net longwave radiation that allows a meaningful  
601 separation between cloudy and clear states with unique distributions of downwelling longwave radiation.  
602 The inability to find a distinction between the clear and cloudy states at the continental interior sites may  
603 be related to the fact that previous studies have noted that the cold, dry atmosphere of the continental  
604 interior of Antarctica is conducive to high, optically thin ice clouds, rather than optically thick liquid or  
605 mixed-phase clouds which are lower and have higher near-surface radiative impacts (Morely et al., 1989;  
606 Town et al., 2005, 2007; Ganeshan et al., 2022). In contrast, the three coastal sites have overlap ratios of  
607 less than 0.5 (0.19 for McMurdo, 0.33 for Neumayer, and 0.46 for Syowa) for net longwave radiation  
608 threshold values that correspond closely to the minimum in the net longwave radiation PDF (Figures S3  
609 to S5), indicating that distinct downwelling longwave radiation distributions exist for cloudy and clear  
610 states at these sites. As such, we will evaluate the frequency of stability regimes for cloudy and clear  
611 conditions at the three coastal sites, but not for the interior sites.

612 Figure 12 shows the frequency of each stability regime for cloudy (solid bars) and clear (hatched  
613 bars) cases for the three coastal sites: McMurdo, Neumayer, and Syowa. At McMurdo (Figure 12a), the  
614 most obvious result is that in the MS, SS, and VSS regimes occur much more frequently during the clear  
615 sky state. This result is consistent with previous observations that clear skies allow for radiative cooling  
616 and the development of strong near surface stability (Stone and Kahl, 1991; Hudson and Brandt, 2005). In  
617 contrast, the NN and WS regimes generally occur preferentially during cloudy conditions, also consistent  
618 with previous results that increased cloud cover reduces near-surface stability (Stone and Kahl, 1991;  
619 Hudson and Brandt, 2005). Interestingly, the VSM and NN-SSA regimes occur nearly equally regardless  
620 of cloud cover. This indicates that changes in downwelling longwave radiation related to varying cloud  
621 cover do not play a dominant role in the forcing of these regimes.

622 When examining the distribution for Neumayer (Figure 12b), the SS regime is over twice as  
623 frequent during clear compared to cloudy conditions, as expected (Stone and Kahl, 1991; Mahrt et al.,  
624 1998; Mahrt, 2014; Solomon et al., 2023). The same is true for the VSS regime, and clear conditions are  
625 present for the singular ESS regime as well. The MS and MS-SSA regimes also occur more frequently  
626 with clear rather than cloudy conditions. The NN regimes usually occur with cloudy compared to clear  
627 conditions. The various VSM and WS regimes have occurrences where sometimes clear, and sometimes  
628 cloudy, periods are dominant. There are also VSM and WS regimes where they are roughly equal. This  
629 suggests that changes in downwelling longwave associated with changes in cloud cover do not play a  
630 primary role in forcing the VSM or WS regimes to occur.

631 Finally, at Syowa (Figure 12c), an interesting pattern emerges, where the frequency of most  
632 stability regimes is similar for both cloudy and clear conditions. This is surprising, given that previous  
633 studies have found weaker stability is favored by cloudy conditions, and stronger stability is favored by  
634 clear conditions. This is not the case at Syowa, and may indicate that changes in downwelling longwave  
635 radiation, associated with cloudy and clear conditions, do not exert a strong control on near surface  
636 stability at this site.



637 Figure 12: The distribution of the various boundary layer stability regimes at McMurdo (a), Neumayer (b), and  
 638 Syowa (c) split into cloudy (left, solid bars) clear (right, hatched) observations in the winter season.

#### 639 4 Discussion and Conclusions

640 SOMs have been used in the results presented above to identify the range of boundary layer  
641 stability profiles at two continental interior and three coastal Antarctic sites (Figures 2, 4, 6, 8 and 10).  
642 Based on the SOM analysis a quantitative boundary layer stability definition was developed and applied  
643 to classify the SOM patterns into unique stability regimes. While several studies have examined general  
644 trends in boundary layer stability at individual sites in Antarctica (Hudson and Brandt, 2005; Cassano et  
645 al., 2016; Silva et al., 2022), or estimated inversion strength empirically (Philpot and Zillman, 1970), no  
646 known study has completed a widespread comparison of the range and seasonality of boundary layer  
647 stability across the continent.

648 The stability regimes present, and frequency of these regimes, differed between the continental  
649 interior sites and the coastal sites. At the interior sites, South Pole and Dome C, strong stability patterns  
650 dominate the SOM consistent with previous studies of near-surface stability on the polar plateau (Hudson  
651 and Brandt, 2005; King and Turner, 1997; Andreas et al., 2000). Twenty seven of 30 patterns at South  
652 Pole (Figure 2) and 28 of 30 at Dome C (Figure 4) have stability between MS and ESS, with potential  
653 temperature gradients in excess of  $30 \text{ K (100 m)}^{-1}$  in several of the SOM profiles. Some of the SOM-  
654 identified profiles at these sites have weaker stability near the surface, with stronger stability aloft, and  
655 these patterns are more common at South Pole (Figure 2, bottom two rows) than at Dome C (Figure 4,  
656 bottom right corner). Finally, there are generally more VSS and ESS patterns in the Dome C SOM (left  
657 two columns) compared to the South Pole SOM (upper left corner), indicating stronger stability at this  
658 site, which was also observed by Hudson and Brandt (2005).

659 In contrast to the interior sites, at the coastal sites, McMurdo (Figure 6), Neumayer (Figure 8),  
660 and Syowa (Figure 10), the SOM profiles are more evenly distributed across NN, VSM, WS, MS, and SS  
661 profiles with only one VSS profile and no ESS profiles. Across all three coastal sites, over half of the  
662 SOM-identified patterns have a potential temperature gradient less than  $1.75 \text{ K (100 m)}^{-1}$ . These gradients  
663 occurred for only two or three patterns at Dome C and South Pole, respectively. This indicates more  
664 favorable conditions for weaker near-surface stability at coastal sites (Phillpot and Zillman, 1970;  
665 Cassano et al., 2016). This clearly distinguishes the boundary layer conditions of the continental interior  
666 sites from those at the coastal sites, as also noted by Lettau and Schwerdtfeger, (1967), Phillpot and  
667 Zillman, (1970), Comiso, (1994), Zhang, et al. (2011), and Cassano et al. (2016). It is also important to  
668 note the common occurrence of enhanced stability above a layer of weaker near-surface stability in the  
669 SOMs for the coastal sites in comparison to the continental interior sites. This phenomenon rarely occurs  
670 in the Dome C SOM, only in the bottom right corner (Figure 4), and across the bottom two rows in the  
671 South Pole SOM (Figure 2), but across many of the SOM profiles for McMurdo (Figure 6) and Neumayer  
672 (Figure 8), and some of the SOM for Syowa as well (Figure 10).

673 The SOM analysis indicates a mean boundary layer depth being much shallower at Dome C (45  
674 m) and South Pole (60 m) compared to the coastal sites (95 m to 120 m). The strong near-surface stability  
675 that is almost always present at the continental interior sites limits the depth and strength of turbulent  
676 mixing, while weaker stability at the coastal sites allows for stronger near-surface turbulence and thus  
677 increased boundary layer depths. This behavior of boundary layer depth is also observed by King and  
678 Turner (1997), who found shallow boundary layers in the continental interior with boundary layer depth  
679 increasing towards the coasts. Pietroni et al. (2012) estimated the wintertime boundary layer height at  
680 Dome C using the bulk Richardson number and found it to be always below 150 m, but usually less than  
681 50 m, and Aristidi et al. (2005) found shallower boundary layer depths at Dome C (less than 50 m)  
682 compared to South Pole, consistent with our results.

683 To further summarize and compare the frequency of occurrence of boundary layer regimes  
684 (defined in Table 2) across the Antarctic continent, Figure 13 and Table S1 provide a summary of the  
685 annual and seasonal characteristics of the near-surface stability and maximum stability below 500 m  
686 across all sites. Figure 13 shows the frequency of the near-surface stability regime groupings (e.g., all  
687 NN, regardless of aloft stability, all VSM, regardless of aloft stability, etc.) and the maximum stability  
688 present in the entire profile, either near surface or above the boundary layer and below 500 m (e.g., the  
689 frequency of the basic near-surface stability regime WS and all -WSA cases, all the MS and -MSA, cases,  
690 etc.). Table S1 lists the frequency of WS and weaker, MS and stronger, and SS and stronger stability near  
691 the surface and for the strongest stability below 500 m.

692 It has been previously described in the literature that, even during austral summer, a temperature  
693 inversion is present nearly constantly (Hudson and Brandt, 2005; Genthon et al., 2013). Other studies,  
694 however, note the possibility of unstable conditions in the summer (King and Connolley, 1997;  
695 Mastrantonio, et al., 1999; Pietroni et al., 2013). Thus, this study posed an opportunity to evaluate the  
696 range of stability present in the summer season across multiple Antarctic sites. Regimes with near-surface  
697 stability WS and weaker (Table S1) are the most common regimes at the interior sites in summer (63.2%  
698 of the time at South Pole and 61.4% of the time at Dome C; Figure 13c, Table S1). However, this weaker  
699 near-surface stability is often capped by stronger stability above the boundary layer, such that when  
700 considering the maximum stability below 500 m, regimes with stability MS and stronger occur 86.7% of  
701 the time at South Pole and 81.9% of the time at Dome C. This indicates that moderate or stronger stability  
702 dominates aloft even though weaker stability occurs most of the time near the surface in the summer. This  
703 observation of enhanced stability above a weakly stable boundary layer has not been widely documented,  
704 much less quantified, especially in the continental interior of Antarctica. While winter at Dome C is  
705 characterized almost entirely by near-surface stability regimes SS and stronger (96.9%), the winter at  
706 South Pole experiences these regimes less often (68.8%; Figure 13g). However, when considering the  
707 maximum stability below 500 m (Figure 13h), this reduced frequency of strong stability near the surface  
708 at South Pole compared to Dome C vanishes and regimes with stability SS and stronger occur nearly  
709 continuously and with similar frequency at both South Pole and Dome C (99.6% and 99.2% of the time,  
710 respectively; Table S1).

711 Across all three coastal sites, WS and weaker near surface stability occurs more than 50% of the  
712 time in all seasons, except for Neumayer in winter (Table S1). In the summer WS and weaker near  
713 surface stability is dominant, occurring 80.1% to 92.1% of the time (Figure 13c, Table S1). However, this  
714 high frequency of WS or weaker stability near the surface is not evident when stability aloft is considered  
715 and WS and weaker stability anywhere below 500 m occurs 42.1 to 59.6% of the time (Figure 13d, Table  
716 S1). This indicates that while weaker near-surface stability is dominant in the summer at the coastal sites,  
717 MS or stronger stability is nearly as frequent as WS or weaker stability above the boundary layer. In the  
718 winter, WS and weaker near surface stability occurs 40% to 53.6% of the time (Figure 13g, Table S1)  
719 indicating a near even split between near neutral to weak stability and moderate or stronger stability near  
720 the surface. In contrast, MS and stronger stability is observed within the lowest 500 m 72.1% to 91.6% of  
721 the time during the winter (Figure 13h, Table S1), indicating that weak near surface stability regimes  
722 usually have enhanced (MS or stronger) stability aloft. At McMurdo, the existence of enhanced stability  
723 above a layer of weaker stability was noted by Dice and Cassano (2022). Additionally, Silva et al. (2022)  
724 described the boundary layer at Neumayer ranging from strong surface-based temperature inversions to  
725 weak inversions near the surface with stronger inversions aloft throughout the year, which is also  
726 observed here. While both Dice and Cassano (2022) and Silva et al. (2022) noted the presence of  
727 enhanced stability above a layer of weaker stability, neither of these studies quantified the occurrence or  
728 seasonality of this phenomenon.

729 Comparing the coastal to the continental sites, near-surface WS and weaker stability regimes are  
730 much more common at the coastal sites (61.3% to 72.4%) compared to the continental interior sites  
731 (13.5% to 27.2%) on an annual basis (Table S1). When considering the maximum stability below 500 m  
732 MS and stronger stability occurs nearly all of the time at the interior sites (96.5 to 96.7% of the time) and  
733 occurs more than half of the time at the coastal sites (56.5% to 76.6% of the time) annually (Table S1).  
734 This is consistent with observations from Zhang et al. (2011) who found that surface-based temperature  
735 inversions are less common along the coasts, as the coastal region is warmer, moister, and windier than  
736 the continental interior, which all reduces near-surface stability.

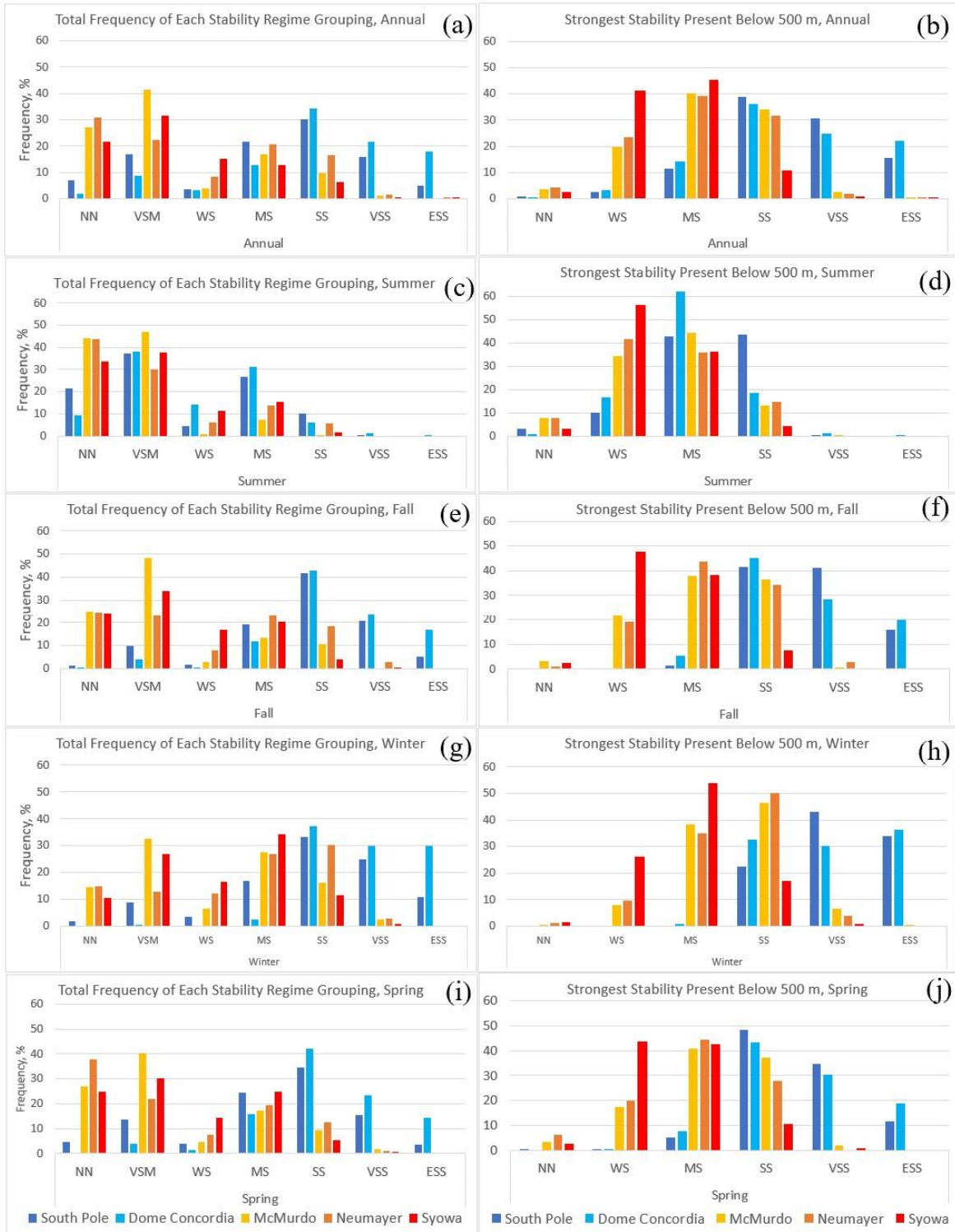
737 In the summer, near-surface stability of WS or weaker occurs most of the time at all sites but is  
738 more frequent at the coastal (80.1% to 92.1% of the time) compared to the continental sites (61.4% to  
739 63.2% of the time) (Table S1). In comparison, near-surface stability regimes SS and stronger only occur  
740 0.5% to 5.9% of the time at the coastal and 7.5% to 10.3% of the time at the interior sites, indicating the  
741 rarity of strong near surface stability at both coastal and interior sites in the summer. However, when also  
742 considering stability just above the boundary layer MS and stronger stability occurs more than 80% of the  
743 time at both South Pole and Dome C (Table S1). Even at the coastal sites, MS and stronger stability  
744 occurs nearly half of the time (40.4 to 57.9%) in the summer (Table S1). These results highlight that  
745 while weak stability is usually present near the surface across the Antarctic continent in the summer,  
746 moderate or stronger stability is often present somewhere in the lowest 500 m of the atmosphere.

747 In the winter, strong stability is expected to be dominant across Antarctica (Lettau and  
748 Schwerdtfeger, 1967; Phillipot and Zillman, 1970; King and Turner, 1997; Andreas et al., 2000).  
749 Surprisingly, the near-surface stability of WS and weaker still occurs 40.0% to 53.6% of the time in the  
750 winter at the coastal sites, whereas these regimes, as expected, are infrequent at the interior sites,  
751 occurring 14.1% of the time at South Pole and 0.8% of the time at Dome C (Figure 13g, Table S1). Near  
752 surface stability stronger than SS occurs 12.3% to 33.4% of the time at the coastal sites and 68.8% to  
753 96.9% of the time at the interior sites (Table S1), emphasizing the dominance of strong near surface  
754 stability in the continental interior in winter. When considering the maximum stability below 500 m, it is  
755 important to note that even though about half the time WS and weaker regimes occur near the surface at  
756 the coastal sites, above the boundary layer enhanced stability remains. MS and stronger stability within  
757 the lowest 500 m of the atmosphere occurs 72.1% to 91.6% of the time at the coastal sites. (Figure 13h,  
758 Table S1). While there are very few cases with WS or weaker near surface stability at the continental  
759 interior sites in the winter these always have enhanced stability above the boundary layer (Figure 13h).  
760 The maximum stability below 500 m at the interior sites is almost always MS and stronger (99.8% to  
761 100%), but in fact, the maximum stability is almost just as often SS or stronger (99.2% to 99.6%) (Table  
762 S1). This emphasizes the near complete dominance of the SS, VSS, and ESS regimes in the continental  
763 interior during the winter, while these regimes represent half or fewer (18.2% to 54.3%) of cases when  
764 considering maximum stability below 500 m at the coastal sites in the winter (Figure 13h, Table S1).

765 It is also interesting to note the frequency of stability regimes in the spring and fall in comparison  
766 to that in the summer and winter at all five sites. At the interior sites, there is a tendency for the regime  
767 frequencies, whether considering just near surface stability or the maximum stability in the lowest 500 m,  
768 in the fall and spring to mirror the winter season regime frequencies, and summer is completely distinct  
769 from the other seasons (Figure 13c through 13j, Table S1). The most common near-surface stability  
770 groupings in the fall and spring are WS and weaker at the coastal sites (55.7% to 71.8% of the time;  
771 Figures 13e and 13i), and these regimes are observed less frequently in the transition seasons than they  
772 are in the summer (80.1% to 92.1%; Figure 13c), but more frequently than in the winter (40% to 53.6%;  
773 Figure 13g). In comparison, the transition seasons at the continental interior sites are usually characterized

774 by MS and stronger stability near the surface (77.7% to 95.4%; Figure 13f and 13j), which is similar to  
775 the frequency of these regimes in the winter as well (85.8% to 99.5%; Figure 13g). Thus, at the interior  
776 sites, this comparison emphasizes the quick descent into the coreless winter from the transition seasons  
777 (Hudson and Brandt, 2005), whereas at the coastal sites, this change is more gradual.





778 *Figure 13: Summary of the basic near-surface stability regime frequency (left column) and aloft stability*  
 779 *regime frequency (right column) at all five sites annually (top row) and seasonally: summer, fall,*  
 780 *winter and spring (bottom four rows). The colored bars indicate the frequency of each of the given regimes at*  
 781 *each site: South Pole (dark blue), Dome C (light blue), McMurdo (yellow), Neumayer (orange), and*  
 782 *Syowa (red).*

783 To assess how applicable the commonly cited clear, strongly stable and cloudy, weakly stable  
784 description of polar winter boundary layers (Stone and Kahl, 1991; Mahrt et al., 1998; Mahrt, 2014;  
785 Solomon et al., 2023) is for the Antarctic we applied the method of Solomon et al. (2023) to identify clear  
786 and cloudy conditions, based on net longwave radiation. This approach for identifying clear and cloudy  
787 conditions was successful at the coastal Antarctic sites (Figures S3 to S5) but was unable to identify  
788 distinct radiative signatures for clear or cloudy conditions at the two interior sites (Figures S1 and S2).  
789 This suggests there may be fundamental differences in processes related to clouds, radiation, and stability  
790 on the polar plateau in comparison to the coastal region of Antarctica or over Arctic sea ice. Vignon et al.  
791 (2017) suggested that there may be two distinct boundary layer regimes (weakly stable and strongly  
792 stable) at Dome C, but contrary to locations in the Arctic (Solomon et al., 2017), this is likely due to a  
793 critical shift in wind speeds, not a bimodal distribution in radiative forcing (Vignon et al., 2017).

794 For the three coastal sites, the frequency of the 20 boundary layer stability regimes defined in  
795 Table 2 was calculated for clear and cloudy conditions (Figure 12). This analysis revealed MS and  
796 stronger regimes occur more often with clear conditions rather than cloudy conditions at McMurdo and  
797 Neumayer. The NN and WS regime grouping at McMurdo (excluding NN-SSA) and the NN regime  
798 grouping at Neumayer occur more often with cloudy rather than clear conditions, but these are the only  
799 stability regimes in this analysis in which there is a large difference in frequency for cloudy or clear  
800 conditions. At Syowa, there is little difference in the frequency of any stability regime for both clear and  
801 cloudy conditions. The fact that some stability regimes at McMurdo and Neumayer and all the stability  
802 regimes at Syowa show little sensitivity to changes in cloud cover suggest a more nuanced relationship  
803 between radiative forcing and near-surface stability may exist in the Antarctic compared to the Arctic, and  
804 other forcing mechanisms, such as mechanical mixing, may be relatively more important in distinguishing  
805 boundary-layer stability regimes from one another. Mahrt (2014) noted that weakly stable conditions  
806 occur with either cloud cover or increased wind and mentioned that classification into the weakly stable  
807 and strongly stable regimes does not encompass the full complexity of forcing in the stable boundary  
808 layer.

809 A useful next step in this research will be to more thoroughly assess the forcing for the different  
810 stability regimes. Largely, radiative forcing and mechanical mixing (wind shear) are two main drivers of  
811 boundary layer stability. The role of these two processes, across seasons at the individual sites, but also  
812 across the five sites will be the basis of continued research. Assessing forcing for regimes that showed  
813 little sensitivity to cloud cover is of interest since it appears that changes in radiative forcing may not play  
814 a dominant role. A paper following this study will use the boundary layer regimes identified for each  
815 individual radiosonde profile to identify variations in radiation and wind speed associated with the  
816 different stability regimes. Further, an analysis of the ability of the Antarctic Mesoscale Prediction  
817 System (AMPS, Powers et al., 2012) to simulate the range of stability regimes observed at each site and  
818 the radiative and mechanical forcing associated with these regimes across Antarctica is planned.

## 819 **Data Availability**

820 The data used to support this project can be found at:

821 McMurdo:

822 All data: [https://adc.arm.gov/discovery/#/results/site\\_code::awr](https://adc.arm.gov/discovery/#/results/site_code::awr).

823 Syowa:

824 Radiosonde data: Office of Antarctic Observation Japan Meteorological Agency (pers. comm.  
825 Yutaka Ogawa)

826 Radiation data: <https://doi.pangaea.de/10.1594/PANGAEA.956748> (Ogawa, et al.)

827 Dome C:

828 Radiosonde data: <https://www.climantartide.it/dataaccess/rds/index.php?lang=it&rds=DOMEC>

829 Radiation data: <https://doi.pangaea.de/10.1594/PANGAEA.935421> (Lupi et al., 2021)

830 South Pole:

831 Radiosonde data: <http://amrc.ssec.wisc.edu/data/ftp/pub/southpole/radiosonde/>

832 Radiation data: <https://doi.pangaea.de/10.1594/PANGAEA.956847> (Riihimaki, et al., 2023)

833 Neumayer:

834 Radiosonde data: <https://doi.org/10.1594/PANGAEA.940584> (Schmithüsen, 2022)

835 Radiation data: <https://doi.org/10.1594/PANGAEA.940584> (Schmithüsen, 2022)

## 836 **Competing Interests**

837 The contact author has declared that none of the authors has any competing interests.

## 838 **Acknowledgements**

839 Funding for this work came from the United States National Science Foundation (NSF) grant OPP  
840 1745097 and the National Aeronautics and Space Administration (NASA; award 80NSSC19M0194). The  
841 authors thank the United States Antarctic Program, the Department of Energy, the Baseline Surface  
842 Radiation Network, the Antarctic Meteorological Research and Data Center, the Antarctic Meteo-  
843 Climatological Observatory, and the Office of Antarctic Observation Japan Meteorological Agency for  
844 the support and logistics for the data used in this paper.

## 845 **References**

846 Andreas, E.L., Claffy, K.J., and Makshtas, A.P.: Low-level atmospheric jets and inversions over the  
847 western Weddell Sea, *Boundary-Layer Meteorology*, 97, 459-486, doi:10.1023/A:1002793831076, 2000.

848 Aristidi, E., Agabi, K., Azouit, M., Fossat, E., Vernin, J., Travouillon, T., Lawrence, J.S., Meyer, C.,  
849 Storey, J.W.V., Halter, B., Roth, W.L., and Walden, V.: An analysis of temperatures and wind speeds  
850 above Dome C, Antarctica, *Astronomy and Astrophysics*, 430, 739-746. doi:10.1051/0004-  
851 6361:20041876, 2005.

852 Comiso, J. C.: Surface temperatures in the polar regions from Nimbus 7 temperature humidity infrared  
853 radiometer, *Journal of Geophysical Research*, 99, 5181-5200. <https://doi.org/10.1029/93JC03450>, 1994.

854 Connolley, W. M.: The Antarctic temperature inversion. *Int. J. Climatol.*, 16, 1333–1342, 1996.

855 Cassano, E.N., Glisan, J.M., Cassano, J.J., Gutowski, W.J. Jr., and Seefeldt, M.W.: Self-organizing map  
856 analysis of widespread temperature extremes in Alaska and Canada, *Climate Research*, 62, 199-218,  
857 <https://doi.org/10.3354/cr01274>, 2015.

858 Cassano, J. J., Nigro, M., and Lazzara, M.: Characteristics of the near surface atmosphere over the Ross  
859 ice shelf, Antarctica, *Journal of Geophysical Research: Atmospheres*, 121, 3339-3362,  
860 <https://doi.org/10.1002/2015JD024383>, 2016.

861 Chechin, D. G., Lüpkes, C., Hartmann, J., Ehrlich, A., and Wendisch, M.: Turbulent structure of the  
862 Arctic boundary layer in early summer driven by stability, wind shear and cloud-top radiative cooling:  
863 ALOUD airborne observations. *Atmospheric Chemistry and Physics*, 23(8), 4685-4707,  
864 <https://doi.org/10.5194/acp-23-4685-2023>, 2023.

865 Dice, M. J., and Cassano, J. J.: Assessing physical relationships between atmospheric state, fluxes, and  
866 boundary layer stability at McMurdo Station, Antarctica, *Journal of Geophysical Research: Atmospheres*,  
867 127, e2021JD036075. <https://doi.org/10.1029/2021JD036075>, 2022.

868 Ganeshan, M., Yang, Y., and Palm, S. P.: Impact of clouds and blowing snow on surface and atmospheric  
869 boundary layer properties over Dome C, Antarctica, *Journal of Geophysical Research: Atmospheres*, 127,  
870 e2022JD036801. <https://doi.org/10.1029/2022JD036801>, 2022.

871 Genthon, C., Six, D., Gallée, H., Grigioni, P., and Pellegrini, A.: Two years of atmospheric boundary  
872 layer observations on a 45-m tower at Dome C on the Antarctic plateau, *Journal of Geophysical Research:*  
873 *Atmospheres*, 118, 3218-3232, doi:10.1002/jgrd.50128, 2013.

874 Handorf, D., Foken, T., and Kottmeier, C.: The stable atmospheric boundary layer over an Antarctic ice  
875 sheet, *Boundary - Layer Meteorology*, 91(2), 165–189, <https://doi.org/10.1023/A:1001889423449> 1999.

876 Hewitson, B. C., and Crane, R. G.: Self-organizing maps: Applications to synoptic climatology, *Climate*  
877 *Research*, 22, 13-26. <https://doi.org/10.3354/cr022013>, 2002.

878 Hudson, S., and Brandt, R.: A look at the surface-based temperature inversion on the Antarctic Plateau,  
879 *Journal of Climate*, 18, 1673-1696, <https://doi.org/10.1175/JCLI3360.1>, 2005.

880 Jozef, G., Cassano, J., Dahlke, S., and de Boer, G.: Testing the efficacy of atmospheric boundary layer  
881 height detection algorithms using uncrewed aircraft system data from MOSAiC, *Atmospheric*  
882 *Measurement Techniques*, 15, 4001-4022, <https://doi.org/10.5194/amt-15-4001-2022>, 2022.

883 Jozef, G. C., Cassano, J. J., Dahlke, S., Dice, M., Cox, C. J., and de Boer, G.: An Overview of the  
884 Vertical Structure of the Atmospheric Boundary Layer in the Central Arctic during MOSAiC, *EGUsphere*  
885 [preprint], <https://doi.org/10.5194/egusphere-2023-780>, 2023.

886 King, J. C., and Connolley, W. M.: Validation of the Surface Energy Balance over the Antarctic Ice  
887 Sheets in the U.K. Meteorological Office Unified Climate Model. *Journal of Climate*, 10(6), 1273-1287.  
888 [https://doi.org/10.1175/1520-0442\(1997\)010<1273:VOTSEB>2.0.CO;2](https://doi.org/10.1175/1520-0442(1997)010<1273:VOTSEB>2.0.CO;2), 1997.

889 King, J. C. and Turner, J.: *Antarctic Meteorology and Climatology*, Cambridge Atmospheric and Space  
890 Sciences Series, Cambridge University Press, U.K., 1997.

891 Kohonen, T., Hynninen, J., Kangas, J., and Laaksonen., J: SOMPAK: The Self-Organizing Map Program  
892 Package, Rep. A31, Lab. Of Comput. and Inf. Sci., Helsinki Univ. of Technol., Espoo, Finland, 1996.

893 König-Langlo, G. and Loose, B.: The Meteorological Observatory at Neumayer Stations (GvN and NM-  
894 II) Antarctica, *Polarforschung*, 76, 25-38, hdl:10013/epic.28566.d001, 2007.

895 Lettau, H. H., and Schwerdtfeger, W.: *Antarctic J. U.S.* 2, 155-158. 1967.

896 Lubin, D., Bromwich, D. H., Vogelmann, A. M., Verlinde, J., and Russell, L. M.: ARM West Antarctic  
897 Radiation Experiment (AWARE) Field Campaign Report, DOE/SC-ARM-17-028, 2017.

898 Lubin, D., Zhang, D., Silber, I., Scott, R. C., Kalogeras, P., Battaglia, A., et al.: AWARE: The  
899 atmospheric radiation measurement (ARM) West Antarctic radiation experiment. *Bulletin of the*  
900 *American Meteorological Society*, 101, E1069-E1091, <https://doi.org/10.1175/BAMS-D-18-0278.1s>,  
901 2020.

902 Lupi, Angelo; Lanconelli, Christian; Vitale, Vito: Basic and other measurements of radiation at Concordia  
903 station (2006-01 et seq). Institute of Atmospheric Sciences and Climate of the Italian National Research  
904 Council, Bologna, PANGAEA, <https://doi.org/10.1594/PANGAEA.935421>, 2021.

905 Mahesh, A., Walden, V. P., and Warren, S. G.: Radiosonde Temperature Measurements in Strong  
906 Inversions: Correction for Thermal Lag Based on an Experiment at the South Pole, *Journal of*  
907 *Atmospheric and Oceanic Technology*, 14, 45-53. [https://doi.org/10.1175/1520-](https://doi.org/10.1175/1520-0426(1997)014<0045:RTMISI>2.0.CO;2)  
908 [0426\(1997\)014<0045:RTMISI>2.0.CO;2](https://doi.org/10.1175/1520-0426(1997)014<0045:RTMISI>2.0.CO;2), 1997.

909 Mahrt, L.: Stratified atmospheric boundary layers and breakdown of models, *Theoretical and*  
910 *Computational Fluid Dynamics*, 11, 263-280, 1998.

911 Mahrt, L.: Stably Stratified Atmospheric Boundary Layers, *Annual review of fluid mechanics*, 46, 23-45,  
912 doi:10.1146/annurev-fluid-010313-141354, 2014.

913 Mastrantonio G., Malvestuto V., Argentini S., Georgiadis T., Viola A.: Evidence of a convective  
914 boundary layer developing on the Antarctic Plateau during the summer, *Meteorology and Atmospheric*  
915 *Physics*, 71:127–132, <https://doi.org/10.1007/s007030050050>, 1999.

916 Matsuoka, K., Skoglund, A., and Roth, G.: Quantarctica [data set]. Norwegian Polar Institute.  
917 <https://doi.org/10.21334/npolar.2018.8516e961>, 2018.

918 Murakoshi, N.: Meteorological observations at the Syowa base during the period from March 1957 to  
919 February 1958, Japan Meteorological Agency, doi/10.15094/00006856, 1958.

920 Nigro, M. A., Cassano, J. J., Wille, J., Bromwich, D. H., and Lazzara, M. A.: A Self-Organizing-Map-  
921 Based Evaluation of the Antarctic Mesoscale Prediction System Using Observations from a 30-m  
922 Instrumented Tower on the Ross Ice Shelf, Antarctica, *Weather and Forecasting*, 32, 223-242,  
923 <https://doi.org/10.1175/WAF-D-16-0084.1>, 2017.

924 Ogawa, Yutaka; Tanaka, Yoshinobu; Ogiyama, Hiroyuki; Fukuda, Masato; Kawashima, Koji; Doi,  
925 Motohisa; Yamanouchi, Takashi: Basic and other measurements of radiation at station Syowa (1994-01 et  
926 seq). National Institute of Polar Research, Tokyo, PANGAEA,  
927 <https://doi.pangaea.de/10.1594/PANGAEA.956748> (dataset in review)

928 Phillipot, H. R., and Zillman, J. W.: The surface temperature inversion over the Antarctic  
929 continent, *Journal of Geophysical Research*, 75, 4161-4169, <https://doi.org/10.1029/JC075i021p04161>,  
930 1970.

931 Pietroni, I., Argentini, S., Petenko, I., and Sozzi, R.: Measurements and Parametrizations of the  
932 Atmospheric Boundary-Layer Height at Dome C, Antarctica. *Boundary Layer Meteorology*, 143, 189-  
933 206, <https://doi.org/10.1007/s1046-011-9675-4a>, 2012.

934 Pietroni, I., Argentini, S., and Petenko, I.: One Year of Surface-Based Temperature Inversions at Dome C,  
935 Antarctica, *Boundary Layer Meteorology*, 150, 131-151,  
936 <https://ui.adsabs.harvard.edu/abs/2014BoLMe.150..131P>, 2013.

937 Powers, J. G., Manning, K. W., Bromwich, D. H., Cassano, J. J., and Cayette, A. M.: A Decade of  
938 Antarctic Science Support Through AMPS, *Bulletin of the American Meteorological Society*, 93, 1699-  
939 1712, doi: <https://doi.org/10.1175/BAMS-D-11-00186.1>, 2012.

940 Reusch, D.B., Alley, R.B., Hewitson, B.C.: Relative performance of self-organizing maps and principal  
941 component analysis in pattern extraction from synthetic climatological data, *Polar Geography*, 29, 188-  
942 212, <https://doi.org/10.1080/789610199>, 2005.

943 Riihimaki, Laura; Long, Charles E; Dutton, Ellsworth G; Michalsky, Joseph: Basic and other  
944 measurements of radiation at station South Pole (1992-01 et seq). NOAA Global Monitoring Laboratory,  
945 Boulder, PANGAEA, <https://doi.org/10.1594/PANGAEA.956847>, 2023.

946 Schmithüsen, Holger: Radiosonde measurements from Neumayer Station (1983-02 et seq). Alfred  
947 Wegener Institute, Helmholtz Centre for Polar and Marine Research, Bremerhaven, PANGAEA,  
948 <https://doi.org/10.1594/PANGAEA.940584>, 2022.

949 Schwartz, B. E., and Doswell, C. A., III.: North American Rawinsonde Observations: Problems,  
950 Concerns, and a Call to Action, *Bulletin of the American Meteorological Society*, 72, 1885-1896,  
951 [https://doi.org/10.1175/1520-0477\(1991\)072<1885:NAROPC>2.0.CO;2](https://doi.org/10.1175/1520-0477(1991)072<1885:NAROPC>2.0.CO;2), 1991.

952 Silber, I., Verlinde, J., Eloranta, E. W., and Cadet, M.: Antarctic Cloud macrophysical, thermodynamic  
953 phase, and atmospheric inversion coupling properties at McMurdo station: I. Principal data processing  
954 and climatology. Antarctic cloud macrophysical, thermodynamic phase, and atmospheric inversion  
955 coupling properties at McMurdo Station: I, Principal data processing and climatology, United States, 123,  
956 6099-6121, <https://doi.org/10.1029/2018JD028279>, 2018.

957 Silva, T., Schlosser, E., and Lehner, M.: A 25-year climatology of low-tropospheric temperature and  
958 humidity inversions for contrasting synoptic regimes at Neumayer Station, Antarctica, *International*  
959 *Journal of Climatology*, 43, 456-479, <https://doi.org/10.1002/joc.7780>, 2022.

960 Solomon, A., Shupe, M.D., Svensson, G., Barton, N.P., Batrak, Y., Bazile, E., Day, J.J., Doyle, J.D.,  
961 Frank, H.P., Keeley, S., Remes, T., Tolstykh, M.: The winter central Arctic surface energy budget: A  
962 model evaluation using observations from the MOSAiC campaign. *Elementa: Science of the*  
963 *Anthropocene*; 11, 00104, doi: <https://doi.org/10.1525/elementa.2022.00104>, 2023

964 Stone, R. S., and Kahl, J. D.: Variations in boundary layer properties associated with clouds and transient  
965 weather disturbances at the South Pole during winter, *Journal of Geophysical Research*, 96, 5137-5144,  
966 doi:10.1029/90JD02605, 1991.

967 Stull, R. B.: *An Introduction to Boundary Layer Meteorology*, Springer, 1988.

- 968 Town, M. S., Walden, V. P., and Warren, S. G.: Spectral and Broadband Longwave Downwelling  
969 Radiative Fluxes, Cloud Radiative Forcing, and Fractional Cloud Cover over the South Pole. *Journal of*  
970 *Climate*, 18(20), 4235-4252. <https://doi.org/10.1175/JCLI3525.1>, 2005.
- 971 Town, M. S., Walden, V. P., and Warren, S. G.: Cloud Cover over the South Pole from Visual  
972 Observations, Satellite Retrievals, and Surface-Based Infrared Radiation Measurements. *Journal of*  
973 *Climate*, 20(3), 544-559. <https://doi.org/10.1175/JCLI4005.1>, 2007.
- 974 Vignon, E., van de Wiel, B. J. H., van Hooijdonk, I. G. S., Genthon, C., van der Linden, S. J. A., van  
975 Hooft, J. A., Baas, P., Maurel, W., Traulle, O., and Casasanta, G.: Stable boundary-layer regimes at Dome  
976 C, Antarctica: observation and analysis, *Quarterly Journal of the Royal Meteorological Society*, 143,  
977 1241, <https://doi.org/10.1002/qj.2998>, 2017.
- 978 Yamada, K., and Hirasawa, N.: of a Record-Breaking Strong Wind Event at Syowa Station in January  
979 2015, *Journal of Geophysical Research: Atmospheres*, 123, 13643-13657.  
980 <https://doi.org/10.1029/2018JD028877>, 2018.
- 981 Zhang, Y., Seidel, D., Golaz, J., Deser, C., and Tomas, R.: Climatological characteristics of Arctic and  
982 Antarctic surface-based inversions, *Journal of Climate*, 24, 5167-5186.  
983 <https://doi.org/10.1175/2011JCLI4004.1>, 2011.